Dynamics of salt intrusion in complex estuarine networks
an idealised model applied to the Rhine–Meuse Delta

Biemond, Bouke; Kranenburg, Wouter M.; Huismans, Ymkje; de Swart, Huib E.; Dijkstra, Henk A.

Important note
To cite this publication, please use the final published version (if applicable).
Please check the document version above.

Ocean Science

Dynamics of salt intrusion in complex estuarine networks: an idealised model applied to the Rhine–Meuse Delta

Bouke Biemond[1], **Wouter M. Kranenburg**[2,3], **Ymkje Huismans**[2,3], **Huib E. de Swart**[1], **and Henk A. Dijkstra**[1]

[1]Department of Physics, Institute for Marine and Atmospheric Research Utrecht, Utrecht University, Utrecht, the Netherlands
[2]Deltares, Delft, the Netherlands
[3]Department of Hydraulic Engineering, Delft University of Technology, Delft, the Netherlands

Correspondence: Bouke Biemond (w.t.biemond@uu.nl)

Abstract. Many deltas in the world consist of a network of connected channels. We identify and quantify the characteristics of salt intrusion in such systems using an idealised model. The Rhine–Meuse Delta is selected as a prototype example of a complex network with many channels. The model is able to capture the characteristics of the tide-dominated water level variations due to the main tidal component and the salinity time series for 1 year of observations. Quantification of tidally averaged salt transport components shows that transport related to exchange flow is dominant in the seaward, deep parts of the network, but tidal dispersion is dominant in shallower channels further inland. Close to the network junctions, a tidally averaged downgradient salt transport is generated by the tidal currents, which is explained by the phase differences between the tidal currents in the different channels. Salt overspill is confined to the most seaward part of the Rhine–Meuse Delta. The magnitudes of the response times of different channels to changes in discharge increase with the distance to the estuary mouth and with decreasing net water transport through the channel. In channels without a subtidal discharge, response times are a factor of 2–4 larger than in the other channels. The effect of changes in the depth on the extent of salt intrusion strongly depends on where the change takes place. If the change is within the salt intrusion range, deepening will locally increase salt intrusion due to an increase in salt transport by the exchange flow. If the change is outside the salt intrusion range, changes to the net water transport dominate the response of the salt intrusion.

1 Introduction

The extent of salt intrusion into estuaries is changing worldwide as a result of climate change and anthropogenic activities. Climate change includes, for example, sea level rise (Qiu and Zhu, 2015) and changes in freshwater discharge (Bellafiore et al., 2021). Examples of anthropogenic activities are dam construction on rivers for water storage and hydropower generation (Qiu and Zhu, 2013), channel deepening for ship navigation, and construction of polders (Liu et al., 2019). The availability of theoretical frameworks to explain and of suitable models to simulate salt intrusion is crucial to predict how these changes affect the extent of salt intrusion.

For single-channel estuaries, relationships between estuarine geometry, forcing conditions, and salt intrusion are extensively studied. For this, theoretical frameworks (Geyer and MacCready, 2014), semi-empirical models (Savenije, 1993), idealised models (MacCready, 2004; Wei et al., 2022), models of intermediate complexity (Dijkstra and Schuttelaars, 2021), and detailed numerical models (Ralston et al., 2010; Martyr-Koller et al., 2017; Liu et al., 2024) are being used.

However, a number of estuaries consist of multiple channels. For these systems, also referred to as estuarine networks, the theories developed for single-channel estuaries need to be extended, as they behave differently in several ways. Observations show (Gong et al., 2014) that tidally averaged salt transport between channels through the junctions, a phenomenon known as salt overspill, occurs. Second, the phasing of tidal currents in estuarine networks creates local minima in the salt field (Warner et al., 2002; Garcia et al., 2022), which challenges the traditional view that salt trans-

port by tides can be considered a dispersive process (Winterwerp, 1983). The implications of these phenomena for the large-scale salt dynamics are hard to determine from observations. Furthermore, unsteadiness of the salt field is known to be important in single-channel estuaries (e.g. Bowen and Geyer, 2003; Banas et al., 2004). For estuarine networks, Biemond et al. (2023) find that the interaction between channels depends on forcing conditions. Observations show that salt intrusion in some channels in the Mekong Delta changes substantially due to variation in tidal forcing over the spring–neap cycle, while other channels are less sensitive (Eslami et al., 2021). Using a 3D model, they explained this from differences in depth and stratification, but the interaction between the channels was not explicitly quantified. Next, the theory about the effect of changes to the geometry of estuaries does not contain all the relevant processes in estuarine networks. For example, Wu et al. (2016) suggest that the deepening of the North Passage, one of the channels of the Yangtze River Estuary, may have contributed to the salinity of the other channels. Liu et al. (2019) mention that channel deepening changed the amount of discharge reaching the Modaomen Waterway in the Pearl River Delta but that local channel deepening was more important to the salt intrusion.

Salt intrusion in estuarine networks has been studied using 1D models, for example, by Nguyen and Savenije (2006) and Zhang et al. (2011). Such models, when calibrated, have proven to be successful at predicting salt intrusion into estuaries, but their simplified nature does not allow the identification of the mechanisms of salt intrusion. On the other hand, 3D models have been used (e.g. Xue et al., 2009; Bricheno et al., 2021; Bellafiore et al., 2021), and while these models typically include realistic geometry and a wide range of physical processes that affect the salt transport, their high computational costs make extensive sensitivity studies computationally unfeasible. To fill the gap between simple 1D models and 3D numerical models of estuarine networks, we develop here an idealised, partly analytical, width-averaged (2DV) model. This model is suitable for a process-based analysis of salt intrusion mechanisms, as the model solves separately for different components of currents and salinity, which makes the computation of different components of the salt transport straightforward. Furthermore, it has lower computational costs than a 3D numerical model and it is easier to implement features such as estuarine network geometry.

To study the characteristics of salt intrusion in estuarine networks, the model will be applied to the Rhine–Meuse Delta (the Netherlands) (RMD), which is formed by the outflow of the Rhine and Meuse rivers discharging into the North Sea (Fig. 1). The current geometry of the delta is to a large extent anthropogenically determined (Cox et al., 2021), with the large harbour of Rotterdam situated in the seaward part. Earlier research on salt intrusion into this system by de Nijs and Pietrzak (2012) using measurements and 3D model simulations revealed that intertidal transport of salt between the channels occurs, but the effects of this transport on the

tidally averaged salinity were not quantified. Recently, salt intrusion into the RMD has received increased attention. Kranenburg et al. (2022) showed that upstream salt transport is dominated by exchange flow in the seaward part and by tidal currents in the landward part of one of the major branches but that during storm surges, the relative importance of the different mechanisms changes. Wullems et al. (2023) point to the dependency of salinity on water level at one location in the network, using a data-driven method. None of these studies provide a network-wide analysis of salt intrusion.

To systematically investigate the dynamics of salt intrusion in estuarine networks, we formulate four specific aims:

1. to show that a calibrated, idealised 2DV model successfully hindcasts hydrodynamics and salinity in an estuarine network;

2. to identify and quantify the different salt transport processes in an estuarine network and highlight the differences from single-channel estuaries;

3. to quantify the time-dependent response to changes in discharge in an estuarine network;

4. to quantify the effects of changes in the depth of individual channels on salt intrusion into the major branches of an estuarine network.

The remainder of this paper is organised as follows. In Sect. 2, the model, its implementation in the RMD, and the set-up of the simulations are described. Section 3 presents results focused on the four specific aims. Section 4 discusses the results, and Sect. 5 presents the conclusions.

2 Model formulation

2.1 Model approach

The model chosen to address the research questions is an exploratory model. This type of model is simplified where possible, such that it only contains the essential ingredients to describe the relevant physics (Murray, 2003). The simplifications aim to isolate poorly understood phenomena, in this case, salt intrusion into estuarine networks. An additional advantage is that due to the lower computational demand, parameter sensitivity studies are easy to perform. Successful examples of this approach in the context of salt intrusion can be found in, for example, MacCready (2004), Chen (2015), and Wei et al. (2016). Detailed quantitative agreement with observations is not the primary goal of this type of models. However, to assure that the right part of the parameter space is investigated, we will calibrate the model parameters using a model–observation comparison. The simplifications in the model primarily concern the geometry, concern the turbulence closure, and disregarded physical processes. In the model description in the remainder of this section, simple
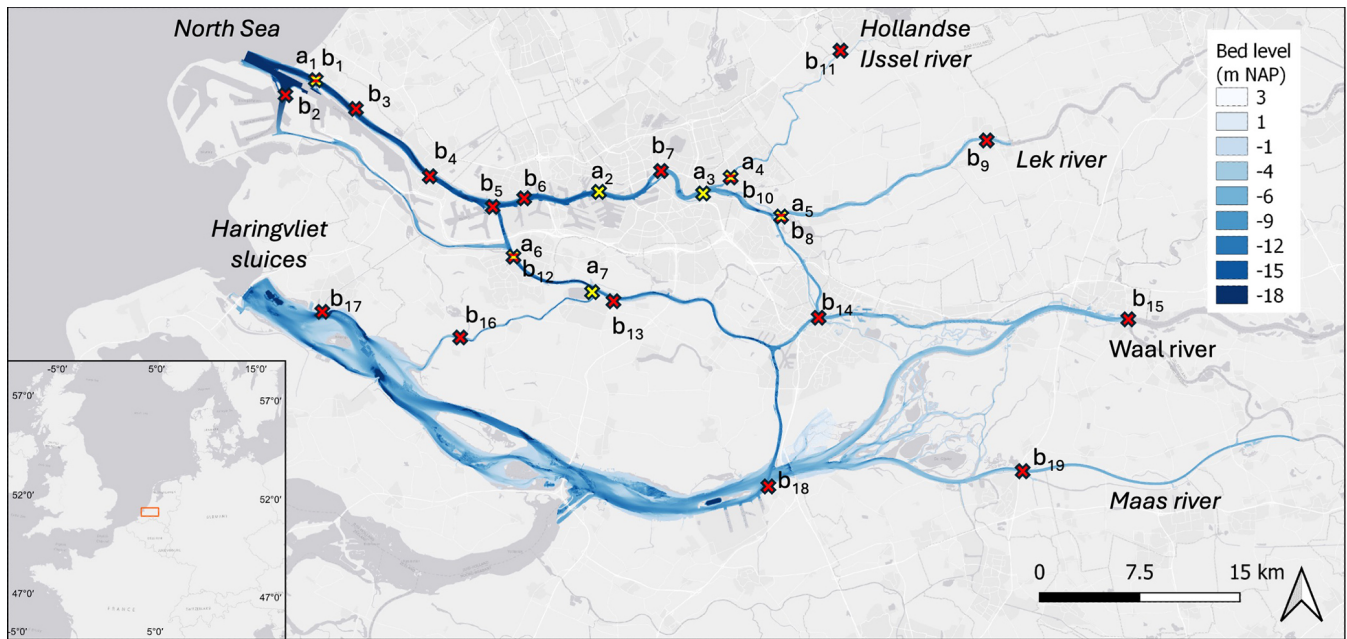
Figure 1. Map of the Rhine–Meuse Delta. The inset shows the location in Europe. The bed level is indicated in Normaal Amsterdams Peil (NAP), which is a measure of the mean sea level. The yellow crosses indicate salinity observation points (a_1–a_8) and the red crosses water level observation points (b_1–b_{19}). Locations where both these quantities are measured or when these observation points are very close together are indicated by both colours.

formulations of these aspects will be used. The consequences of the assumptions on which these formulations are built will be addressed in the discussion section.

2.2 Domain

The domain mimics an estuarine network that has a number of width-averaged channels, which are connected to each other through a set of junctions. As a specific example, Fig. 2 shows the representation of the RMD network. There are four types of horizontal boundaries for the channels: river boundaries, weir boundaries, sea boundaries (estuary mouths), and junctions. Salt enters through the sea boundaries. Fresh water enters (or leaves, for example, in the case of the Haringvliet sluices) through the river and weir boundaries. The junctions provide the connections between the channels.

Each channel i is divided into a number of segments j, which have different constant depths H_{ij}. Locations in the segments are characterised by a horizontal coordinate x_{ij}, which runs from $-L_{ij}$ to 0, and by a vertical coordinate z_{ij} that runs from the bottom $z_{ij} = -H_{ij}$ to the water surface $z_{ij} = \eta_{ij}$, while the undisturbed water level is at $z_{ij} = 0$. By convention, x_{ij} increases in the direction of the time- and cross-sectionally averaged flow for yearly averaged discharge conditions (indicated by arrows in Fig. 2). For clarity, the subscript ij will be left out from now on, and the equations shown are valid for each segment. The width of each

segment is described as

$$b(x) = b(x = -L)e^{(x+L)/L_b}, \tag{1}$$

where L_b is an e-folding length scale that describes the width convergence. The width is continuous at the boundaries of the segments but not necessarily at the junctions.

2.3 Equations of motion

The governing equations for hydrodynamics and salinity are described in Biemond et al. (2024a). The model is width averaged, and in this domain, momentum and continuity balances are solved for hydrodynamics, and a mass balance is solved for salinity. Water level η, horizontal and vertical velocity u and w, and salinity s are decomposed into tidally varying (indicated by the subscript ti) and subtidal (indicated by the subscript st) components. Subtidal horizontal velocity and salinity are further decomposed into a depth-averaged component (indicated by an overbar) and a depth-dependent component (indicated by a prime). This yields

$$\eta = \eta_{\text{st}} + \eta_{\text{ti}}, \quad u = \overline{u}_{\text{st}} + u'_{\text{st}} + u_{\text{ti}},$$
$$w = w_{\text{st}} + w_{\text{ti}}, \quad s = \overline{s}_{\text{st}} + s'_{\text{st}} + s_{\text{ti}}. \tag{2}$$

Analytical solutions to the dominant tidally averaged momentum and mass balances are found, which yield expressions for the subtidal water level gradient $\frac{\partial \eta_{\text{st}}}{\partial x}$, the depth-averaged and depth-varying components of the subtidal hor-
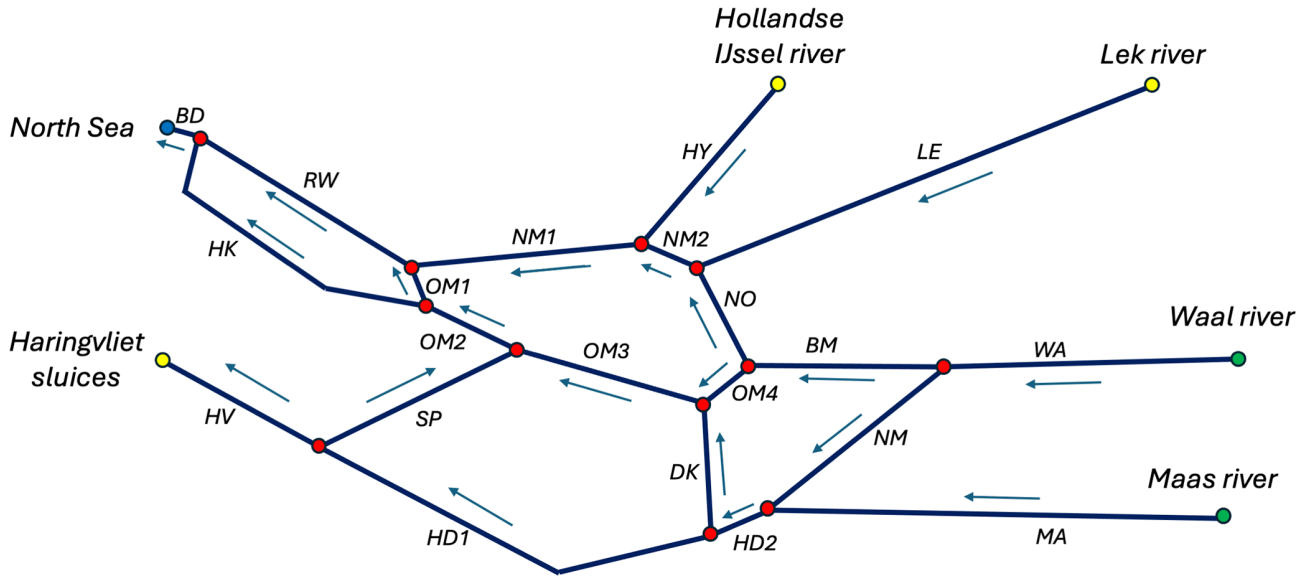
Figure 2. Representation of the RMD channel network in the model. Black lines indicate channels, blue arrows indicate the direction of the local x axis, red dots indicate junctions, yellow dots indicate weir boundaries, green dots indicate river boundaries, and blue dots indicate sea boundaries. Table A1 provides the meaning of the acronyms for the channels.

izontal velocity u_{st} and vertical velocity w_{st}. They read

$$\frac{\partial \eta_{st}}{\partial x} = -\frac{6}{5}\frac{A_{v,st}Q}{gbH^3}, \tag{3a}$$

$$\bar{u}_{st} = \frac{Q}{bH}, \tag{3b}$$

$$u'_{st} = \frac{Q}{bH}P_1(\tilde{z}) + \frac{g\beta H^3}{48A_{v,st}}\frac{\partial \bar{s}_{st}}{\partial x}P_2(\tilde{z}), \tag{3c}$$

$$w_{st} = -\frac{g\beta H^4}{48A_{v,st}}\left(\frac{\partial^2 \bar{s}_{st}}{\partial x^2} + L_b^{-1}\frac{\partial \bar{s}_{st}}{\partial x}\right)P_w(\tilde{z}). \tag{3d}$$

Here, Q is net water transport, $g = 9.81\,\mathrm{m\,s^{-2}}$ is gravitational acceleration, $\beta = 7.6 \times 10^{-4}\,(\mathrm{g\,kg^{-1}})^{-1}$ is the isohaline contraction coefficient, and $A_{v,st}$ is the vertical eddy viscosity acting on the subtidal flow. The quantity $\frac{\partial \eta_{st}}{\partial x}$ is required to calculate the water distribution in the channels, and similarly, w_{st} is required for the vertical structure of the subtidal salinity field s'_{st}. Note that we have neglected the contribution of salinity to the subtidal water level gradient because taking it into account would introduce a strong relationship between salinity and net water transport, which is not realistic (Buschman et al., 2010; Maicu et al., 2018; Wang et al., 2021). Polynomials P_1, P_2, and P_w describe the vertical structure of the flow and depend on the normalised vertical coordinate $\tilde{z} = \frac{z}{H}$. They are defined as

$$P_1(\tilde{z}) = \left(\frac{1}{5} - \frac{3}{5}\tilde{z}^2\right), \quad P_2(\tilde{z}) = \left(\frac{8}{5} - \frac{54}{5}\tilde{z}^2 - 8\tilde{z}^3\right),$$

$$P_w(\tilde{z}) = \left(2\tilde{z}^4 + \frac{18}{5}\tilde{z}^3 - \frac{8}{5}\tilde{z}\right). \tag{4}$$

The water level η_{ti}, horizontal velocity component u_{ti}, and vertical velocity component w_{ti} of the tidally varying flow field read

$$(\eta_{ti}, u_{ti}, w_{ti}) = \Re\{(\hat{\eta}_{ti}, \hat{u}_{ti}, \hat{w}_{ti})\exp(i\omega t)\}, \tag{5a}$$

$$\hat{\eta}_{ti} = \exp\left(-\frac{(x+L)}{2L_b}\right)$$
$$\quad\quad (C_1\exp(k(x+L)) + C_2\exp(-k(x+L))), \tag{5b}$$

$$\hat{u}_{ti} = \frac{g}{i\omega}\frac{\partial \hat{\eta}_{ti}}{\partial x}\left(B\cosh\left(\delta_A\frac{z}{H}\right) - 1\right), \tag{5c}$$

$$\hat{w}_{ti} = i\omega\hat{\eta}_{ti} - \frac{g}{i\omega}\left(\frac{d^2\hat{\eta}_{ti}}{dx^2} + \frac{1}{L_b}\frac{d\hat{\eta}_{ti}}{dx}\right)$$
$$\quad\quad \left(\frac{BH}{\delta_A}\sinh(\delta_A\frac{z}{H}) - z\right). \tag{5d}$$

Here, ω is the angular frequency of the tidal constituent that is considered, t is time, L is the length of a channel segment, $\Re$ denotes the real part of a complex variable, and C_1 and C_2 are determined by the horizontal boundary conditions and represent tidal waves that travel downstream and upstream, respectively. The other parameters are defined as

$$\delta_A = \frac{(1+i)H}{\sqrt{\frac{2A_{v,ti}}{\omega}}}, \quad B = \left(\cosh(\delta_A) + \frac{\delta_A}{2}\sinh(\delta_A)\right)^{-1},$$

$$k = \sqrt{\frac{1}{(2L_b)^2} + \frac{\omega^2}{gH}\left(\frac{B}{\delta_A\sinh(\delta_A)} - 1\right)^{-1}}, \tag{6}$$

in which $A_{v,ti}$ is the vertical eddy viscosity acting on the tidal flow. Note that we split subtidal horizontal velocity into a

depth-averaged and a depth-dependent component but do not make this separation for tidal velocity. Furthermore, $A_{v,ti}$ and therefore u_{ti} do not depend on salinity.

For salinity, no analytical expressions are obtained, but the decomposition from Eq. (2) is substituted in the 2DV mass balance for salinity, which reads

$$\frac{\partial s}{\partial t} + \frac{1}{b}\frac{\partial}{\partial x}(bus) + \frac{\partial}{\partial z}\left(ws\right)$$
$$= \frac{1}{b}\frac{\partial}{\partial x}\left(bK_h\frac{\partial s}{\partial x}\right) + \frac{\partial}{\partial z}\left(K_v\frac{\partial s}{\partial z}\right). \quad (7)$$

Here, K_h is the horizontal dispersion coefficient, and K_v is the vertical eddy diffusivity coefficient. To obtain an equation for subtidal depth-averaged salinity $\bar{s}_{st}$, we average this equation over depth and the tidal timescale, which gives

$$\frac{\partial \bar{s}_{st}}{\partial t} + \bar{u}_{st}\frac{\partial \bar{s}_{st}}{\partial x} + \overline{u'_{st}\frac{\partial s'_{st}}{\partial x}} + \left(\bar{u}_{ti}\frac{\partial \bar{s}_{ti}}{\partial x}\right)_{st} + \overline{\left(u'_{ti}\frac{\partial s'_{ti}}{\partial x}\right)}_{st}$$
$$= \frac{1}{b}\frac{\partial}{\partial x}\left(bK_{h,st}\frac{\partial \bar{s}_{st}}{\partial x}\right). \quad (8)$$

In this expression, $K_{h,st}$ is the horizontal dispersion coefficient acting on the subtidal salinity. The equation for the vertically varying part of the subtidal salinity s'_{st}, obtained from subtracting Eq. (8) from the tidally averaged mass balance, reads

$$\frac{\partial s'_{st}}{\partial t} + \bar{u}_{st}\frac{\partial s'_{st}}{\partial x} + u'_{st}\frac{\partial \bar{s}_{st}}{\partial x} + u'_{st}\frac{\partial s'_{st}}{\partial x} - \overline{u'_{st}\frac{\partial s'_{st}}{\partial x}} + w_{st}\frac{\partial s'_{st}}{\partial z}$$
$$+ \left(\bar{u}_{ti}\frac{\partial s'_{ti}}{\partial x}\right)_{st} + \left(u'_{ti}\frac{\partial \bar{s}_{ti}}{\partial x}\right)_{st} + \left(u'_{ti}\frac{\partial s'_{ti}}{\partial x}\right)_{st}$$
$$- \overline{\left(u'_{ti}\frac{\partial s'_{ti}}{\partial x}\right)}_{st} + \left(w_{ti}\frac{\partial s'_{ti}}{\partial z}\right)_{st}$$
$$= \frac{1}{b}\frac{\partial}{\partial x}\left(bK_{h,st}\frac{\partial s'_{st}}{\partial x}\right) + \frac{\partial}{\partial z}\left(K_{v,st}\frac{\partial s'_{st}}{\partial z}\right). \quad (9)$$

Here, $K_{v,st}$ is the vertical eddy diffusivity coefficient acting on the subtidal salinity. An equation for tidally varying salinity s_{ti} is obtained by subtracting the tidally averaged mass balance from the full mass balance. Additionally, only the dominant tidal constituent is considered, i.e. $s_{ti} = \Re\left[\hat{s}_{ti}\exp(-i\omega t) + c.c.\right]$, and a scaling analysis is applied to select the most important terms. The equation governing the dynamics of $\hat{s}_{ti}$ is

$$-i\omega\hat{s}_{ti} + \hat{u}_{ti}\frac{\partial \bar{s}_{st}}{\partial x} + \hat{w}_{ti}\frac{\partial s'_{st}}{\partial z} = \frac{\partial}{\partial z}\left(K_{v,ti}\frac{\partial \hat{s}_{ti}}{\partial z}\right), \quad (10)$$

in which $K_{v,ti}$ is the vertical eddy diffusivity coefficient acting on the tidally varying salinity. This equation has an analytical solution (i.e. $\hat{s}_{ti}$ can be expressed as a function of s_{st}), but this expression is very lengthy and therefore not presented here. To numerically solve for $\bar{s}_{st}$ and s'_{st}, a Galerkin

method is used in the vertical and central differences in the horizontal. For time integration, a backward Euler scheme is employed.

The values of the vertical eddy viscosity, vertical eddy diffusivity, and horizontal dispersion coefficients are assumed to be constant throughout the entire domain. For bottom friction, a partial slip condition is applied at the bed, with a friction coefficient $S_f = \frac{2A_v}{H}$, where A_v is the vertical eddy viscosity, and H is the water depth. Note that the values of the coefficients used for eddy viscosity, eddy diffusivity, dispersion, and friction depend on whether they act on the tidal or subtidal current and salinity, as is explained in, for example, Godin (1991, 1999).

2.4 Salt transport

The horizontal salt transport T in the model (which follows from the decomposition of currents and salinity as in Eq. 2), integrated over the tidal cycle and cross-section and after neglecting terms that contain η (see Biemond et al., 2024a), reads

$$T = \underbrace{Q\bar{s}_{st}}_{T_Q} + \underbrace{bH\overline{u'_{st}s'_{st}}}_{T_E} + \underbrace{bH\overline{(u_{ti}s_{ti})}_{st}}_{T_T} - \underbrace{bHK_{h,st}\frac{\partial \bar{s}_{st}}{\partial x}}_{T_D}. \quad (11)$$

The component T_Q is the salt transport due to advection by the depth-averaged subtidal current, T_E is the salt transport by the exchange flow, T_T is the salt transport due to the time correlation of tidal flow and salinity, and T_D is the salt transport due to horizontal dispersion. In our model, unresolved upstream salt transport processes are parametrised by the last term. Note that T_T could be further decomposed into a contribution that involves only the depth-averaged tidal current and a contribution that is due to the departure of the tidal current from its depth-averaged value.

2.5 Boundary conditions

Regarding the boundary conditions at river boundaries, subtidal discharge is prescribed, tides are assumed to dissipate in the river beyond the boundary (without reflection at a horizontal boundary), and the subtidal salinity is set to the river salinity. Hence,

$$bH\bar{u}_{st} = Q_{riv}, \quad C_1 = 0, \quad \bar{s}_{st} = s_{riv}, \quad s'_{st} = 0. \quad (12)$$

Here, Q_{riv} and s_{riv} are the river discharge and salinity, respectively, which are generally non-zero. The condition $C_1 = 0$ means that there is no downstream travelling tidal wave.

At the weir boundaries, we prescribe subtidal discharge and use a reflecting boundary condition for the tidal flow such that the water transport vanishes at such boundaries. For salinity, we impose conditions on the salt transport. When the discharge at the weir is into the domain (which is usually the case), the depth-averaged transport equals the prescribed salinity s_{weir} multiplied by the discharge. When the

discharge at the weir is out of the domain (which is the case for the Haringvliet sluices in the RMD, for example), the depth-averaged transport is set to the calculated salinity at the weir multiplied by the discharge. The vertical variations in the dispersive salt flux are set to zero to avoid the formation of a dispersive boundary layer (Biemond et al., 2024b). In summary, the boundary conditions read

$$bH\overline{u}_{st} = Q_{weir}, \quad \int_{-H}^{0} u_{ti}dz = 0,$$

$$T = Q_{weir}s_{weir}, \quad K_{h,st}\frac{\partial s'_{st}}{\partial x} = 0, \quad (13)$$

in which Q_{weir} is the discharge at the weir, and s_{weir} is prescribed in the case of the discharge being from the weir and is the local (depth-averaged) salinity in the case of a discharge towards the weir.

Water levels η_{st} and η_{ti} are prescribed at sea boundaries (estuary mouths). To obtain the conditions for salinity, additional segments are added that extend seaward from the mouths. These segments are characterised by strongly increasing widths away from the mouths. At the outer sea boundaries of these segments, salinity is set to the sea salinity. Furthermore, the assumption that there is only an incoming tidal wave at these locations (i.e. travelling from sea to estuary) allows us to compute the water levels and tidal flow in these segments. The assumption made here is reasonable because of the strongly increasing width of these segments.

At the junctions, continuity of discharge and water level is imposed. These conditions apply to the subtidal quantities as well as to the tidally varying quantities. Regarding salinity, continuity of salt transport and salinity is used at every vertical level. To apply conditions to the tidal salinity, a boundary layer correction is employed. At the boundaries between the channel segments, the same conditions are applied. The specific expressions for these boundary conditions are described in Appendix B, and the boundary layer correction for tidal salinity is described in Appendix C.

2.6 Model implementation for the RMD

The implementation of the domain of the RMD in the model, as sketched in Fig. 2, consists of 21 channels, 12 junctions, 1 sea boundary, 3 weir boundaries, and 2 river boundaries. The channels consist of one or two segments. The division into multiple segments is based on the desired horizontal grid size and does not affect the physics. The Haringvliet sluices connect the Haringvliet to the open sea and are only opened to release water from the Haringvliet such that no salt intrudes through this boundary. The widths and depths of each channel are presented in Table A1. Note that a coarse representation of the geometry is used, so geometrical details (e.g. the harbour basins) are not resolved. In the following, we will refer to the different channels by the acronyms specified in Fig. 2.
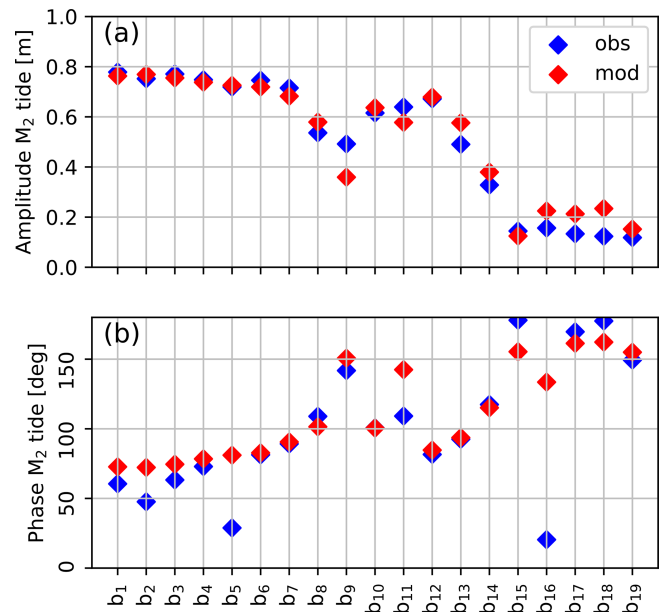
Figure 3. (a) Observed (in blue) and modelled (in red) amplitudes of the M_2 water level for different points in the RMD, the locations of which are indicated in Fig. 1. **(b)** As **(a)**, but for the tidal phase of the water level.

The horizontal grid size is around a few hundred metres but differs per channel and is finer in regions where larger salinity gradients are expected. In the vertical, five Fourier modes are used for the Galerkin projection, and the model time step (which only applies to subtidal quantities) is 24 h.

The model is forced with prescribed time series of discharge at the two river and the three weir boundaries and with the water level amplitude and phase of the dominant tidal constituent, which is the semi-diurnal lunar M_2 tide (period 12 h, 25 m) for the RMD at the North Sea boundary (note that the water level amplitude of the M_2 component at the station at the mouth (b_1) is 4 times larger than that of the second-largest component; Walters, 1987). For salinity, time-independent values are used, which are $0.15\,\mathrm{g\,kg^{-1}}$ at the river and weir boundaries and $33\,\mathrm{g\,kg^{-1}}$ at the North Sea boundary.

3 Results

3.1 Model–observation comparison

3.1.1 Method

To address the first aim (model–observation comparison), suitable values of eddy viscosity, eddy diffusivity, and dispersion coefficients are needed. This is achieved by means of calibration: the modelled tidal water levels and salinities are compared to observed tidal water levels and salinities. There are 19 water level stations in the RMD, indicated by b_1–b_{19}

in Fig. 1, and 7 salinity observation points, indicated by a_1–a_7 in this figure. At a number of these locations, salinity observations are available at two or three depths. There are only a few permanent current measurement stations available in the RMD, and therefore currents are not evaluated. The discharge, water level, and salinity data of the RMD are accessible at https://waterinfo.rws.nl, last access: 31 January 2024. The year 2022 is used as calibration period since this is a year with a low Rhine discharge, which is a situation in which salt intrusion is relevant. For the hydrodynamic module, the vertical eddy viscosity component acting on the tidal flow $A_{v,ti}$ is calibrated. An optimisation procedure is employed for this variable to find the minimum error between the modelled and the observed M_2 water level variations, using the skill score as used by Davies and Jones (1996), which computes a cost function f as

$$f = \sum_{k=1}^{N} \sqrt{\left(\hat{\eta}_k^{\mathrm{obs}} - \hat{\eta}_k^{\mathrm{mod}}\right)^2 + 2\hat{\eta}_k^{\mathrm{obs}}\hat{\eta}_k^{\mathrm{mod}}\left(1 - \cos\left(\hat{\theta}_k^{\mathrm{obs}} - \hat{\theta}_k^{\mathrm{mod}}\right)\right)}. \quad (14)$$

Here, N is the number of observations; $\hat{\eta}_k^{\mathrm{obs}}$ and $\hat{\eta}_k^{\mathrm{mod}}$ are the observed and modelled amplitudes of the water level of the dominant tidal constituent, respectively; and $\hat{\theta}_k^{\mathrm{obs}}$ and $\hat{\theta}_k^{\mathrm{mod}}$ are the observed and modelled phases of the tidal water level, respectively.

The coefficients for subtidal vertical eddy viscosity $A_{v,st}$, subtidal vertical eddy diffusivity $K_{v,st}$, horizontal dispersion $K_{h,st}$, and tidal vertical eddy diffusivity $K_{v,ti}$ are calibrated by minimising the root-mean-squared error (RMSE) between observed and modelled time series of subtidal salinity at the observations points. A gradient descent algorithm is employed to find the optimal values of these parameters. After the calibration, the model performance regarding subtidal salinity is quantified by calculating the Nash–Sutcliffe efficiency (NSE) (Nash and Sutcliffe, 1970), which reads

$$\mathrm{NSE} = 1 - \frac{\sum_{k=1}^{N}\left(s_k^{\mathrm{obs}} - s_k^{\mathrm{mod}}\right)^2}{\sum_{k=1}^{N}\left(s_k^{\mathrm{obs}} - <s_k^{\mathrm{obs}}>\right)^2}, \quad (15)$$

where s_k^{obs} and s_k^{mod} are the observed and modelled salinity, respectively, and $< \cdot >$ indicates a time-averaged quantity. A score of $\mathrm{NSE} = 1$ indicates perfect agreement, while $\mathrm{NSE} = 0$ means that the model error is equal to the variance of the observed time series, and finally $\mathrm{NSE} < 0$ indicates that the observed mean is a better predictor than the model.

3.1.2 Tides

The amplitudes and phases of the M_2 component of the water level in observations and of the calibrated model are shown in Fig. 3. A minimum for f is obtained with $A_{v,ti} = 0.025\,\mathrm{m^2\,s^{-1}}$. The amplitude in the main channels is well-resolved (b_1–b_7, b_{12}–b_{14}). At observation point b_9 (the LE channel), the amplitude is underestimated by 27 %, and in the southern part (b_{16}–b_{19}), the amplitude is overestimated

by 55 % averaged over the four points. There are two outliers in terms of tidal phases (at points b_5 and b_{16}). The observed phase at point b_5 differs in such a way from the phase at the neighbouring points that an error in the raw data is probably responsible for the mismatch here. At point b_{16}, the tides are affected by the operation of the Haringvliet sluices, which is not resolved in the model.

3.1.3 Salinity

The NSE (Eq. 15) for the modelled and observed salinity after calibration is 0.67, which classifies the model performance as satisfactory (Moriasi et al., 2015). This result is found for $A_{v,st} = 0.0024\,\mathrm{m^2\,s^{-1}}$, an order of magnitude lower than the vertical eddy viscosity for tidal flow. Regarding vertical eddy diffusivities for tidal and subtidal salinity, the best agreement is found when using $K_{v,st} = \frac{A_{v,st}}{Sc}$ and $K_{v,ti} = \frac{A_{v,ti}}{Sc}$, with Sc, the Schmidt number, equal to 2.2. The horizontal subtidal dispersion coefficient is $K_{h,st} = 275\,\mathrm{m^2\,s^{-1}}$, which is rather high compared to what was found for single-channel estuaries (Biemond et al., 2024a). The reasons for and implications of this will be discussed in Sect. 4.

Modelled and observed salinity in the RMD at four selected observation points is shown in Fig. 4. We refer to Fig. S1 for the comparison at the other observations points. Differences between the model and observations primarily concern an underestimation of the variability in the salt field. This is due to the fact that our model does not account for the spring–neap tidal cycle, overtides, and subtidal and intratidal water level fluctuations at the sea boundary driven by remote winds, which have a strong influence on the variability in the salinity. The model–data agreement is consistent at different depths for most stations where observations are available at multiple depths (Fig. S1), but the salinity at station a_1 is underestimated by $3.0\,\mathrm{g\,kg^{-1}}$ at $z = -9.0\,\mathrm{m}$ averaged over first 2 months of the year (i.e. during high-discharge conditions), while at $z = -2.5\,\mathrm{m}$, no bias is present (compare Fig. S1b with Fig. S1d). This indicates that the relation between discharge and vertical salinity gradients in the model is not well resolved, which is probably due to the use of a constant vertical eddy viscosity and vertical eddy diffusivity. In Fig. 4b, we see an underestimation of $0.6\,\mathrm{g\,kg^{-1}}$ averaged over the summer months, while in Fig. 4d, which is only a few kilometres from this location, the salinity is overestimated by $0.4\,\mathrm{g\,kg^{-1}}$ during this period. This probably originates from the large value of $K_{h,st}$, which reduces horizontal salinity gradients, but the exclusion of other tidal constituents besides M_2 also plays a role, as tidal flow is very important to salinity at point a_4, which will be shown in the next section.
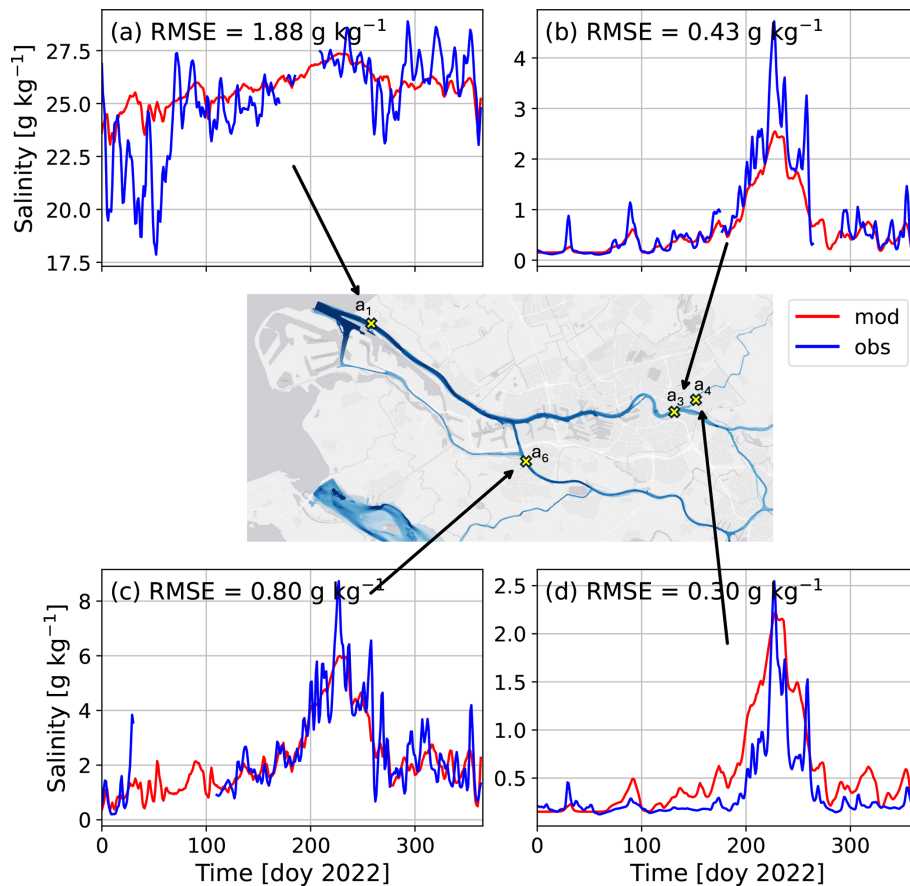
Figure 4. Observed (in blue) and modelled (in red) tidally averaged salinity time series for 2022 at four locations in the RMD: **(a)** a_1 ($z = -9.0$ m), **(b)** a_3 ($z = -2.5$ m), **(c)** a_6 ($z = -2.5$ m), and **(d)** a_4 ($z = -4.0$ m).

## 3.2 Salt intrusion mechanisms

3.2.1 Method

To quantify the mechanisms of salt transport in an estuarine network (the second research aim), an equilibrium simulation is performed with the calibrated model. To this end, the model is forced with discharges that represent low-discharge conditions, as this is the situation in which salt intrusion is the most relevant. For the Haringvliet sluices and the Hollandse IJssel and Lek rivers, we set the discharge to zero, while for the Waal River, we use $Q = 650$ m^3 s^{-1} and for the Maas River, $Q = 50$ m^3 s^{-1}. These values equal approximately the minimum observed discharges in the summer of 2022.

The distribution of net water transport and subtidal salinity in different channels in the RMD is presented in Fig. S2; the associated components of the salt transport in different channels in the RMD for low-discharge conditions are shown in Fig. 5.

3.2.2 Main channels

It turns out that close to the sea boundary (BD, RW), salt transport related to the exchange flow T_E is the most important contribution to the salt transport, while further inland its relative contribution decreases. This spatial pattern is explained by the fact that close to the sea boundary, depth is large, but further inland, the RMD becomes shallower (e.g. $H = 16$ m for BD and RW but $H = 11$ m for NM1 and $H = 10.2$ m for OM3). The strength of the exchange flow u'_{st} scales with H^3 (Eq. 3c), and the variable s'_{st}, which is mainly generated by this flow, thus decreases when depth decreases (Fig. S3). The salt transport component T_E is the product of those two and therefore strongly depends on depth.

The salt transport component due to horizontal dispersion T_D becomes dominant in most areas where T_E declines (e.g. NM1, SP, OM3). This is because the dependence of T_D on depth is weaker (only through a decrease in the cross-section).
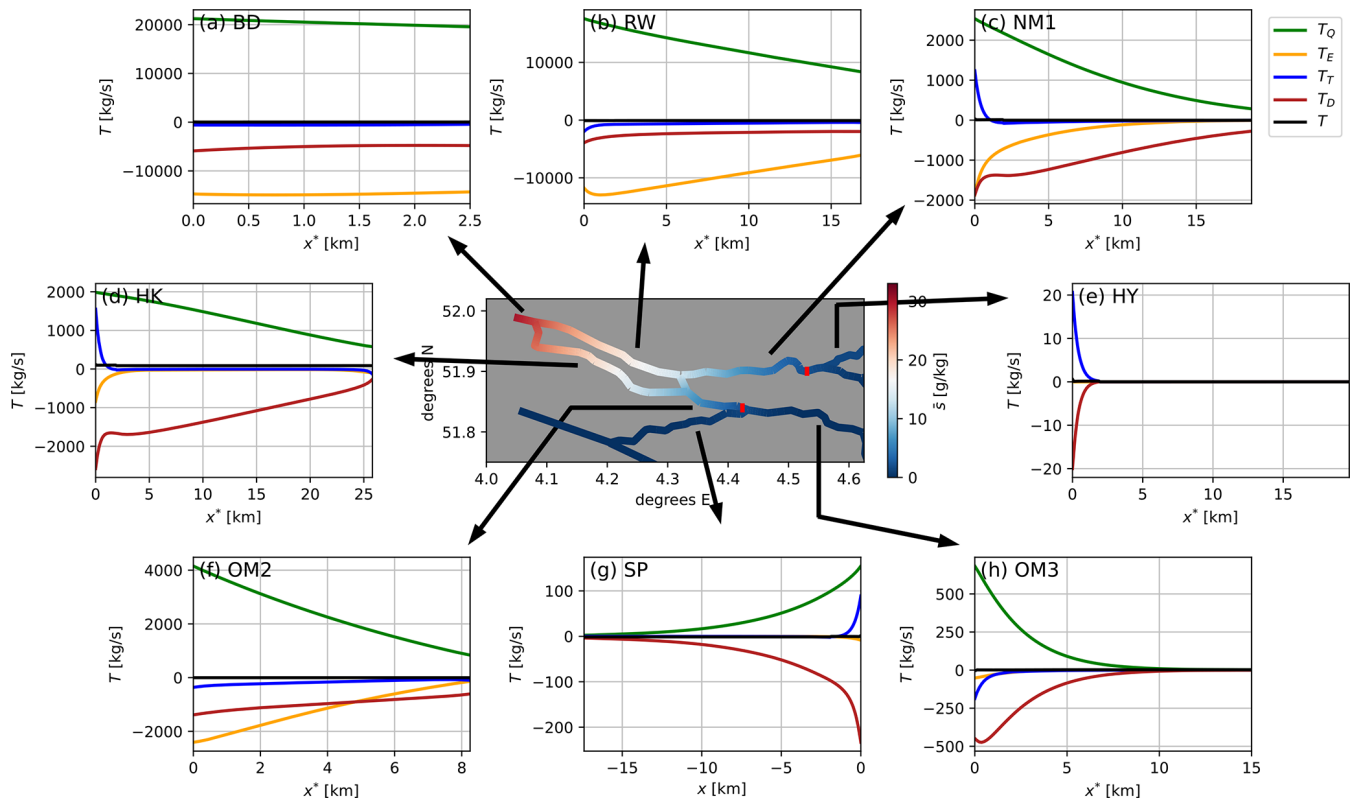
Figure 5. The centre panel shows depth and tidally averaged salinity in the RMD for low-discharge conditions. The red bars in this figure indicate the location of the $2\,\mathrm{g\,kg^{-1}}$ isohaline. **(a–h)** The different components of the salt transport in equilibrium, following the decomposition of Eq. (11), versus x or x^*, where we have defined $x^* \equiv -x$ for plotting purposes.

3.2.3   Tidal transport

The component due to tides (T_T) is small in most of the network. To explain this, we compute the phase difference between depth-averaged tidally varying flow and salinity, which is very important to the magnitude of T_T (see Eq. 11). A phase difference of more (less) than $90°$ is associated with upstream (downstream) salt transport. In our model context, this phase difference is generated by two mechanisms: vertical advection of subtidal salinity within the tidal cycle (Biemond et al., 2024a) and interaction with other channels around junctions. The first mechanism requires the presence of tidally averaged vertical salinity gradients, which are mainly are created by the exchange flow. This gives, for example, a phase difference of about $95°$ in the RW (Fig. S4), which yields $T_\mathrm{T} \approx 500\,\mathrm{kg\,s^{-1}}$, about 15 times smaller than T_E. Note that a T_T of this strength would be the dominant salt transport in channels further upstream (e.g. OM3). In the channels where exchange flow is weaker, the phase difference that is induced is also smaller, and therefore T_T is a subdominant component of the salt transport except around some junctions. The net salt transport due to vertical variations in the tidally varying flow and salinity is not considered

for this explanation because its contribution to salt transport is negligible, as explained in Biemond et al. (2024a).

3.2.4   Transport in the vicinity of junctions

Near junctions such as the SP–OM2–OM3 or the BD–RW–HK, the distortion of the phase difference from $90°$ increases strongly, for example, around the seaward boundary of the HK, NM1, and HY, where the minimum phase difference is about $60°$ (Fig. S4). Here, T_T also reverses sign (i.e. it turns seaward) along the salinity gradient. Note that for each junction in only one connected channel is the phase difference below $90°$. To illustrate this behaviour, we study the case of the junction of the HY, NM1, and NM2 in detail, but similar reasoning applies to the other junctions. Figure 6 visualises tidal currents and salinity around this junction. Figure 6a shows that $\overline{u}_\mathrm{ti}$ in the HY leads the currents in the other two channels by about 1.5 h. The consequences for the salt transport are made clear by studying the different phases of the tide. When the currents in all channels are positive (i.e. the red shaded area and panel 1), relatively fresh water from upstream is transported downstream, and salinity at the junction decreases (Fig. 6b). At some point, the current in the HY will change direction before the currents in the other channels change direction (the blue shaded area and panel 2). In

this phase, the HY will receive freshwater from upstream, i.e. from the NM2. After about 1.5 h, currents in the other channels will also change direction (the light blue area and panel 3), and saline water from downstream is imported into the channels. However, when salinity at the junction reaches its maximum value, $\overline{u}_{\mathrm{ti}}$ in the HY has already changed direction (the yellow area and panel 4), and this salinity does not reach the HY. The tidally averaged transport T_{T} is upstream in the main channels (NM1 and NM2), while it is downstream in the side channel (HY).

3.2.5 Minor channels

The HY (and also the LE) is a special case in the sense that it does not receive discharge from upstream, and therefore T_Q is zero throughout this channel. The absence of discharge, which is the main source of buoyancy, also implies that (tidally averaged) vertical salinity gradients are almost absent: the top–bottom salinity difference is 0.09 g kg^{-1} at 1 km from the junction in the HY. This implies that T_{E} is weak (i.e. $\frac{T_{\mathrm{E}}}{T_{\mathrm{D}}} = 5 \times 10^{-4}$) at this location.

A similar situation occurs in the HK, which is shallower than its neighbouring channels: it receives less discharge (71 m^3 s^{-1}; about 9 times smaller than the RW) and is consequently less stratified, and the channel-averaged contribution of T_{E} to the upstream salt transport in the HK is only 4 % (Fig. 5d).

3.2.6 Overspill

The absolute value of the total salt transport $|T|$ is 80 kg s^{-1} in the HK, OM1, and RW, indicating the presence of salt overspill in these channels. Overspill occurs when salt originating from one channel is transported downstream with the subtidal current $\overline{u}_{\mathrm{st}}$ through another channel. In Fig. S2, the direction of this transport is indicated. For the range of values of the parameters investigated in this study, this only occurs in the RW–OM1–HK channel system in the RMD. Under the low-discharge conditions studied here, its contribution to the total salt transport in the HK is 13 %.

3.3 Response to changes in discharge

3.3.1 Method

To examine the response of salinity in the network to changes in discharge (the third research aim), the model is forced with discharge time series that represent the transition from reference discharge conditions to low-discharge conditions and vice versa. For the Haringvliet sluices and the Hollandse IJssel River, discharge is set to zero. In the reference situation, the Lek, Waal, and Maas rivers are forced with their yearly average discharge, which is 490, 1500, and 230 m^3 s^{-1}, respectively. To simulate the response to a transition to low-discharge conditions, the reference discharges are multiplied by a factor ranging from 0.95 to 0.2 for the different scenar-

ios. In this way, the fraction of the total discharge received per channel does not change. The simulation is continued until equilibrium has been reached. To simulate the response to an increase in river discharge, discharge is increased from the lowered value to the yearly average values, and again the simulation is continued until equilibrium has been obtained. Note that these simulations do not reproduce the current water distribution in the RMD during a drought because discharge into the three rivers does not change according to the same ratio due to water management and local differences in drought intensity. Moreover, the Haringvliet sluices are opened when the discharge is high, closed for low discharge, and partially opened in between.

To quantify the salinity response to a change in discharge, studies of single-channel estuaries have analysed the evolution of a certain isohaline, typically the 2 g kg^{-1} isohaline (Chen, 2015; Monismith, 2017). However, in a network this is not generally possible, as isohalines are not bound to a certain channel. Therefore, an alternative measure for the salt intrusion into a channel is used for response times, which is based on the channel-averaged salinity S, defined as $S = \frac{\int_V s_{\mathrm{st}} \mathrm{d}V}{V}$, where V is the volume of the channel. The response time is then defined as when 90 % of the change in S has occurred (note that S becomes constant after the change in discharge). We indicate the time it takes to respond to a low discharge as τ_{dry} and the time it takes to respond to a high (i.e. the reference) discharge as τ_{wet}.

3.3.2 General behaviour

The changes in mean salinity and the response times of individual channels in the RMD after an increase or decrease in the discharge of the Lek, Waal, and Maas rivers are shown in Fig. 7. A larger change in discharge is associated with a larger change in mean salinity, as was expected. The absolute changes in salinity are larger for channels close to the sea (RW, HK) but smaller for channels close to the limit of the salt intrusion (SP, HY, OM3). Regarding response times, τ_{dry} increases for larger changes in discharge (the τ_{dry} associated with an 80 % change in discharge is 61 % larger than the τ_{dry} of a 5 % change for the channels considered in Fig. 7), but τ_{wet} is not sensitive to the magnitude of the change in discharge (the τ_{wet} associated with an 80 % change in discharge is only 9 % larger than the τ_{wet} of a 5 % change for the channels considered in Fig. 7). This implies that τ_{dry} and τ_{wet} differ little for small changes in discharge but that τ_{dry} exceeds τ_{wet} for larger changes in discharge.

Following Biemond et al. (2022), who also found this result for single-channel estuaries, the explanation is that τ_{dry} equals the change in salt content, which scales with the change in salinity, divided by salt import due to T_{E} and T_{D}, which depend on the salinity gradient during the adjustment. The change in salinity and salinity gradient are in a different manner related to the change in discharge, and therefore τ_{dry} depends on the change in discharge. On the other hand, τ_{wet}
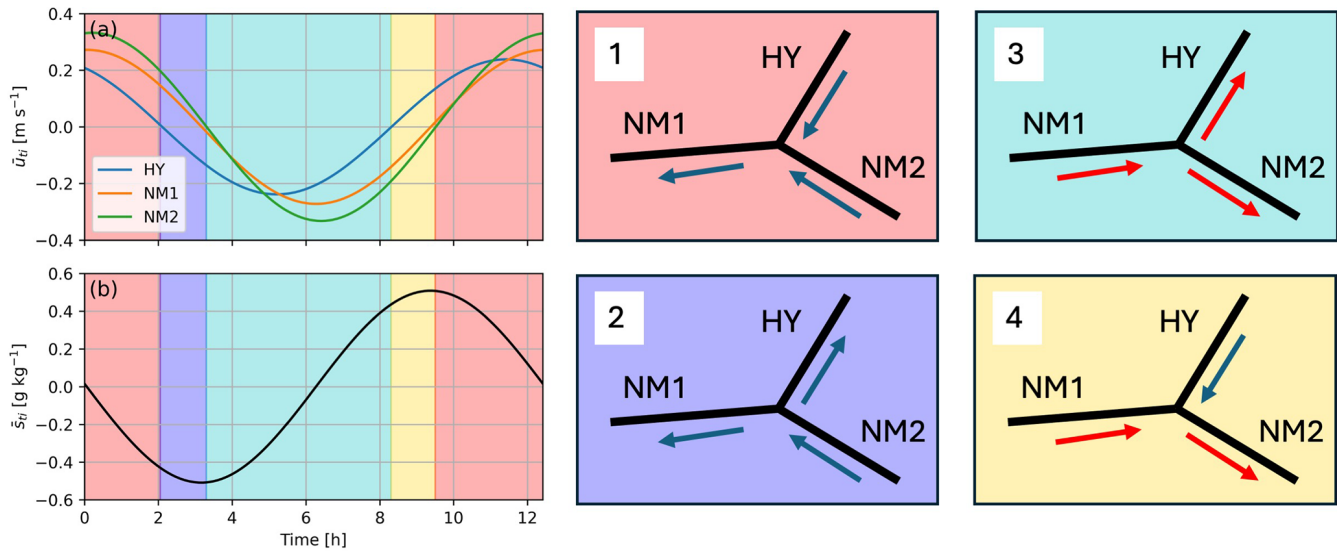
Figure 6. (a) Depth-averaged tidal velocity $\overline{u}_{ti}$ within a tidal cycle at the junction of the Hollandse IJssel (in blue), Nieuwe Maas 1 (in orange), and Nieuwe Maas 2 (in green). **(b)** As **(a)**, but for depth-averaged tidal salinity $\overline{s}_{ti}$. Panels 1–4 show the visualisation of the situation during different phases of the tide. The background colours correspond to the colours of panels **(a)** and **(b)**. The arrows indicate the direction of the current, and the colour indicates whether the water is relatively fresh (blue) or relatively saline (red).

is mostly determined by the change in salt content divided by the export of salt due to T_Q, which both scale linearly with salinity, and therefore their ratio does not depend on the change in discharge.

The channels closer to the estuary mouth, i.e. those with high salinity (RW, NM1), have a smaller τ_{dry} than the channels with low salinity (HY, SP). This is because channels with higher salinity also have larger horizontal and vertical salinity gradients (Figs. S3 and S5), which increases the magnitude of the salt import by T_E and T_D.

3.3.3 Minor channels

The HK and HY have larger response times than their neighbouring channels. We focus first on the HK, for which τ_{dry} is a factor of 2 higher than in the RW, despite the salinity and salinity gradients being comparable. To explain this, we calculate the total change in salt content in this channel, which equals the channel volume V multiplied by the change in its average salinity, ΔS, divided by its salt import in equilibrium at the downstream boundary ($\tau_r = \frac{V \Delta S}{T_E + T_D + T_T}$), which is a lower bound of τ_{dry}. The salt exchange at the upstream boundary is a factor of 6 smaller in this channel (Fig. 5d) and therefore is not taken into account here. We find $\tau_r = 18.4\,\text{h}$ for the HK, $\tau_r = 4.0\,\text{h}$ for the NM1, and $\tau_r = 3.0\,\text{h}$ for the OM2, for comparison. Thus, the ratio of salt exchange with the neighbouring channels to the total change in salt content in the HK is smaller than for neighbouring channels, which is because this channel receives little discharge, and this explains the larger τ_{dry}. The same reasoning holds for the fact that the τ_{wet} of this channel is larger than in its neighbours,

as in equilibrium the salt import equals the salt export, and therefore the salt export is also relatively small.

3.3.4 Closed channels

In the HY, τ_{dry} is about a factor of 2 higher than that of the other channels. In channels without net water transport like the HY, equilibrium with the forcing conditions will be reached when the horizontal salinity gradient is zero in the channel interior, i.e. when the salinity at the upstream boundary equals the salinity just outside the boundary layer around the junction. This means that the salt front has to intrude over the full length of the channel, which makes the response time larger than for channels with net water transport. Moreover, only the salt transport component T_D (see Sect. 3.2) imports salt into this channel during the adjustment process, while T_T exports salt around the junction (Fig. 5e). The high τ_{dry} of the HY and more generally of channels without discharge is thus explained by the fact that salt import by T_E is absent and that salt has to intrude over the full length of the channel.

Figure 7c shows that τ_{wet} is also high in the HY. This is because there is no discharge through the channel that flushes the salinity (through T_Q). Instead, salt is removed by T_D and T_T. As for the other channels, τ_{wet} is smaller than τ_{dry} in the HY, but different mechanisms than in most other channels play a role here. First, T_T has the same sign as T_D in the boundary layer around the junction when salinity in the channel decreases, so salt export during a decrease in salinity is faster than salt import during an increase in salinity. Second, the salinity in the channels that the HY is connected to
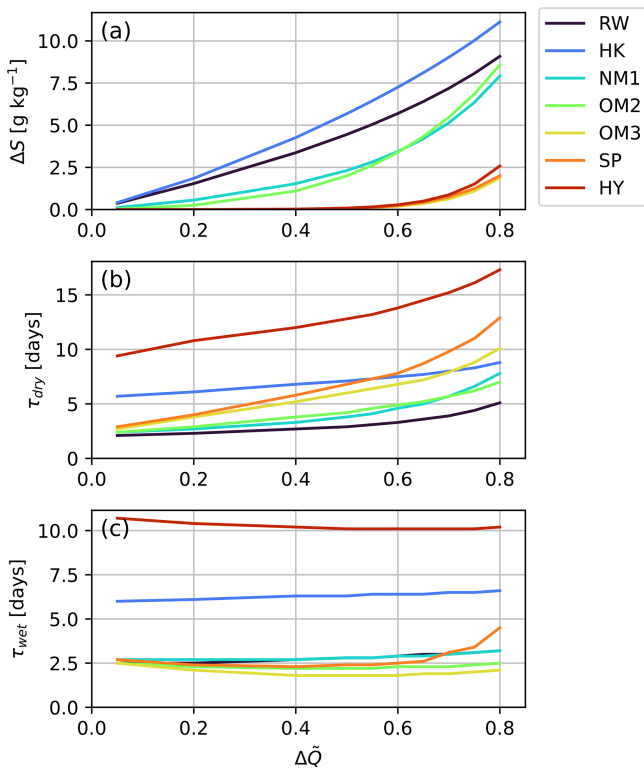
Figure 7. **(a)** Absolute value of the change in channel-averaged salinity ΔS of different channels as a function of the change in discharge $\Delta \tilde{Q} = \frac{Q_{\mathrm{ref}} - Q_{\mathrm{dry}}}{Q_{\mathrm{ref}}}$, where Q_{ref} is the yearly average discharge and Q_{dry} the decreased discharge. Note that ΔS is independent of the sign of the change in discharge because absolute values are considered. **(b)** As **(a)**, but for the response time τ_{dry} due to a decrease in river discharge, i.e. a transition from Q_{ref} to Q_{dry}. **(c)** As **(b)**, but for the response time τ_{wet} due to an increase in river discharge, i.e. a transition from Q_{dry} to Q_{ref}.

responds faster to an increase in discharge than to a decrease in discharge (compare τ_{wet} and τ_{dry} of NM1).

3.4 Response to changes in depth

3.4.1 Method

Effects of changes to the depth of individual channels on salt intrusion in the major branches (the fourth research aim) are quantified by analysing the output of a set of equilibrium simulations that have the same forcing conditions as the simulation for the second research aim. In each of these simulations, the depth of one of the channels in the network is increased or decreased by 25 %. The impact on the salt intrusion is quantified by means of the distance X_2 from the RW–NM1–OM1 junction to the subtidal $2\,\mathrm{g\,kg}^{-1}$ isohaline in the Nieuwe Maas (consisting of channels NM1 and NM2) and in the Oude Maas (consisting of channels OM1, OM2, OM3, and OM4), the two major branches of the network. The locations of these isohalines are shown in the centre panel of

Fig. 5. These quantities can be converted into the distance to the sea boundary by adding the length of the BD and of the RW, which is 19.3 km in total.
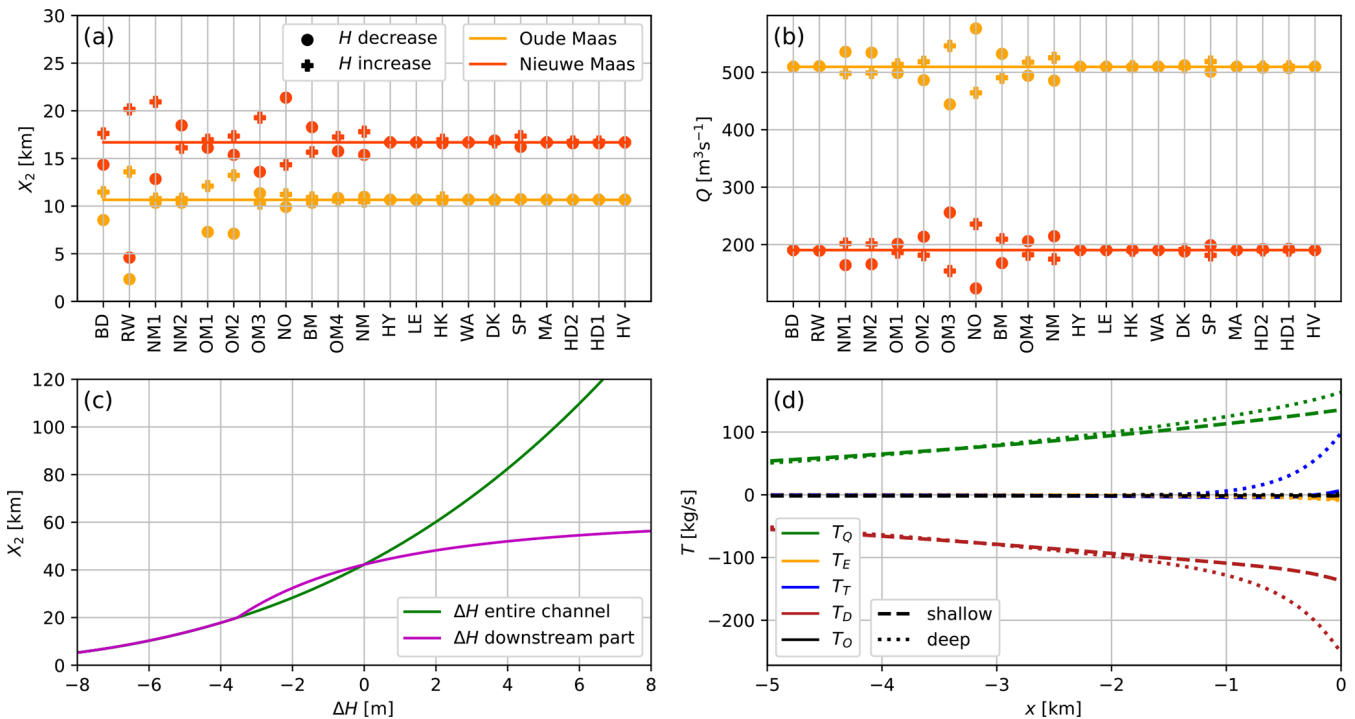
Salt intrusion lengths X_2 of the Oude Maas and Nieuwe Maas for changes in the depth of individual channels are shown in Fig. 8a. In contrast to the simulations for Sect. 3.3, the net water transport distribution changes when the depth changes, and the values for the major branches are presented in Fig. 8b. The responses of the salt intrusion lengths range from no detectable change in X_2 to a maximum change of 12 km. In the following, we will explain the mechanisms that are responsible for the different responses.

3.4.2 Seaward channels

Changes in the depth of the most seaward channels (BD and RW) affect the extent of the salt intrusion (increases when deepening, decreases when shoaling) because upstream salt transport in these channels is dominated by T_E (Fig. 5a), which depends strongly on the local depth (Sect. 3.2). Changing the depth of the RW has a larger effect on X_2 than changing the depth of the BD because the RW is longer.

The magnitude of the change in X_2 due to a decrease $+\Delta H$ in depth exceeds the change after an increase $-\Delta H$. Scaling relations between the depth and extent of the salt intrusion in single-channel estuaries (Monismith et al., 2002) predict a scaling with H^3 when T_E is the dominant salt import mechanism, which implies that, in contrast to what we find, an increase in depth would result in a larger absolute change in X_2 rather than a decrease.

To understand why the scaling is different in a network, a simple model for the RW is constructed, which mimics the RW as a single-channel estuary but with two segments and assumes a balance between T_Q and T_E (the Chatwin, 1976, balance), which are the dominant salt transport components in the RW (Fig. 5b). The details of the model are in Appendix D. In this case, analytical solutions for the salt intrusion length as a function of depth are obtained. Two scenarios are considered: in the first, the depth of the entire channel is changed. In the second, only the depth of the downstream 20 km long segment of the channel is changed. The results are shown in Fig. 8c. When the depth of the entire channel is changed (the green line), an increase in depth has a larger impact than a decrease in depth, which follows from the previously mentioned H^3 scaling (Eq. D2). However, when the depth of only the downstream part of the channel is changed (the purple line), a deepening $+\Delta H$ has a smaller effect than shoaling $-\Delta H$. This is because when the depth is increased, the salt intrusion length increases, and only a limited part of the salt intrusion experiences a larger depth and the associated increase in salt transport. In the case of shoaling, the salt intrusion length decreases, and a relatively large part of the salt intrusion experiences a smaller depth and the related decrease in salt transport. As the RW and BD are within the

Figure 8. (a) The salt intrusion length X_2, defined as distance from the RW–NM1–OM1 junction to the $2\,\mathrm{g\,kg^{-1}}$ isohaline in the Oude Maas (yellow) or Nieuwe Maas (red) versus the changes in depth of different channels. The dots indicate a decrease in depth, and the plus markers indicate an increase in depth. The lines indicate X_2 with the current geometry. **(b)** As **(a)**, but for the net water transport through OM1 (yellow) and NM1 (red). **(c)** Salt intrusion length X_2 of a single-channel estuary that consists of two segments as a function of change in depth ΔH of the entire estuary (green) or change in depth of the downstream 20 km (purple) around a reference depth of 16 m (the depth of the RW), using Eqs. (D4) and (D5). **(d)** As Fig. 5g, but for a shallower HD1 (dashed line) or a deeper HD1 (dotted line) and zoomed in on the 5 km of the channel adjacent to the SP–OM2–OM3 junction.

range of salt intrusion, increasing their depth has a smaller effect than decreasing their depth.

3.4.3 Main channels

For changes to the depth of channels that are a part of the major branches Oude Maas and Nieuwe Maas, two competing mechanisms play a role. The first is that deepening increases the magnitude of T_E. The second mechanism is that, simultaneously, the net water transport through the branch will increase due to a decrease in friction, causing an increase in T_Q. Because of volume conservation, the magnitude of the change in net water transport is equal to that of the other major branch but with the opposite sign. The change in friction when changing the depth also affects the tidal currents, but the changes in the salt transport component T_T are negligible. The interplay of these mechanisms means that when deepening channels that are part of the major branches and are within the limit of the salt intrusion (i.e. the NM1, OM1, and OM2), salt intrusion increases. This is because locally the magnitude of T_E increases, which dominates the increase in T_Q. In the other major branch, salt intrusion increases as well because net water transport decreases (Fig. 8b). On the

other hand, changing the depth of the channels that are part of the major branches but outside the limit of the salt intrusion (NM2, OM3) does not affect T_E directly but only T_Q. This means that an increase in depth decreases salt intrusion into the major branch that the channel is part of and simultaneously increases salt intrusion into the other major branch. Note that the statements in this section are given for deepening. For shoaling, we find the opposite effect. Changes in net water transport also explain the response of channels that are important for the distribution of the Waal River discharge (i.e. the NO, BM, OM4, and NM). The NO in particular has a large effect on salt intrusion into the Nieuwe Maas, as this channel exerts a strong control on the amount of discharge from the Waal River that reaches the Nieuwe Maas. The salt intrusion into the Nieuwe Maas is more sensitive to changes in net water transport than that into the Oude Maas because the net water transport through the Nieuwe Maas is about 2.5 times smaller than that through the Oude Maas (Fig. 8bf).

3.4.4 Other channels

Changes in the depth of the other channels in the RMD (HY in Fig. 8a and all channels to its right) have little impact on

X_2 in the Nieuwe Maas and Oude Maas (changes are less than 1 km). There are, however, two cases that have an interesting local effect. The first concerns a change in depth in the HK. In the reference simulation, salt overspill occurs in the HK ($T = 80 \, \text{kg s}^{-1}$), and salt from the Oude Maas is transported seawards through the HK (Figs. 5d and S2). When decreasing its depth, the magnitude of the salt transport due to salt overspill increases ($T = 540 \, \text{kg s}^{-1}$), but when increasing the depth, the sign of T reverses, and the HK becomes a source of salt for the Oude Maas ($T = -250 \, \text{kg s}^{-1}$). The consequence of this change in salt transport for the salt intrusion length is only a few hundred metres because this salt transport is relatively weak compared to the amount of salt transported from the RW into the Oude Maas. The second interesting behaviour concerns an increase or decrease in the depth of the HD1. These have little impact on X_2 in the Oude Maas and Nieuwe Maas but affect the extent of the salt intrusion into the SP. The distance of the $0.5 \, \text{g kg}^{-1}$ isohaline in the SP from the junction with the OM2 and OM3 is 6.3, 5.2, and 4.8 km for the shallow, reference, and deep HD1, respectively, so shoaling the HD1 affects salt intrusion more than deepening. To understand this, we calculate the change in salt transport components T_Q and T_T (the flow associated with these components of the salt transport directly changes in the SP due to a change in the depth of the HD1). The difference in T_Q is about $30 \, \text{kg s}^{-1}$ between the shallow and deep HD1. Figure 5g shows that for the reference depth, T_T in the SP close to its seaward boundary is positive; in other words, the salt transport due to tidal currents is directed towards the SP–OM2–OM3 junction. Figure 8d shows that this situation persists for a deep HD1, but when decreasing the depth of HD1, the magnitude of T_T decreases due to a shift in phases of the tidal currents of the different channels around this junction. The difference in T_T at the junction is about $90 \, \text{kg s}^{-1}$, 3 times larger than the change in T_Q, indicating that the change in tidal currents dominates the change in salt intrusion into the SP when deepening the HD1.

4 Discussion

4.1 Comparison with observations

When our idealised network model is applied to the RMD and calibrated against observations, it has a Nash–Sutcliffe efficiency of 0.67. This indicates that the model performance with regard to simulating salinity is satisfactory despite the fact that the descriptions of the physics, forcing conditions, and bathymetry are rather simple. The gradient descent algorithm to find optimal values of the calibration coefficients is crucial to obtain satisfactory model performance.

The effects of the non-resolved aspects of the salinity dynamics on the salt transport are via the calibration mostly projected onto horizontal salt dispersion. A value of $K_{h,st} = 275 \, \text{m}^2 \, \text{s}^{-1}$ is found, and with this value T_D, the tidal dispersion, is the dominant salt transport component in parts of the RMD, in particular around the limit of the salt intrusion. However, since most of the observation points are in the larger channels of the network, this value of tidal dispersion mainly represents the unresolved salt transport in these channels. A hint that in the smaller channels of the network this constant value is too large follows from the described difference in model–data agreement between points a_3 and a_4 (see Sect. 3.1). Model extensions that could possibly resolve this disagreement are discussed in Sect. 4.4.

4.2 Changes in discharge

We found that response times vary between the channels and attributed this to differences in the salinity gradients, the volume/transport ratios of the channels, and the presence of net water transport in the channels. Observations show that response times to changes in forcing are 10–14 d for the HY (Laan et al., 2021), in line with what we find. In another estuarine network, the Po Delta, differences in response times between the channels are minor (Bellafiore et al., 2021, Fig. 5a). This is because in that delta, all channels receive a considerable fraction of the river discharge, and differences in channel depth are also relatively small compared to those in the RMD. Therefore, dynamics of features such as the side branches, like the HY in the RMD, do not play a role in the Po Delta. Certain aspects of the theory of the response of single-channel estuaries to changes in river discharge can be transferred to estuarine networks, for example, the reason for the asymmetry in the response to an increase or decrease in discharge. However, a direct comparison with single-channel estuaries is hindered by factors such as differences in definitions of response times, for reasons that were explained in Sect. 3.3.

4.3 Changes in depth

We showed that in a network, the response of the salt intrusion to changes in depth is sensitive to which channel is changed. Salt intrusion can decrease locally when parts of an estuarine network are deepened due to a redistribution of the river water. This is different for single-channel estuaries, for which it is found that salt intrusion increases when the depth increases (Ralston and Geyer, 2019; Siles-Ajamil et al., 2019; Kolb et al., 2022). Liu et al. (2019) also reported effects on salt intrusion when discharge changes upstream in a network (the Pearl River Delta) due to alterations in the depth. For the Yangtze Estuary, Zhu et al. (2006) reported that salt intrusion increased in multiple channels when the depth of one the channels was increased, in line with what we find for the RMD. Huismans and Plieger (2019) showed, using a 3D model of the RMD, that a shallower Oude Maas leads to a decrease in salt intrusion in the Nieuwe Maas as well as in the Oude Maas. However, when winds and storm surges are accounted for, a more complicated response to

changes in depth occurs. They hypothesised that changes in phases of the currents around the junction could be important to the response to changes in depth; we showed that they indeed can play an important role. For a deepening of the RW, Laan et al. (2023) found that salt intrusion in the entire RMD changes, but when deepening the LE, the effect remains local, which is again in line with what we find.

4.4 Future research

As explained in Sect. 2.1, certain model aspects are highly simplified, which limits the range of simulated salt dynamics in estuarine networks. The fact that only one tidal constituent is considered and that the balances for tidal flow and salinity are simplified implies that not all processes contributing to salt transport by the tidal current are included. Also, the vertical eddy viscosity, vertical eddy diffusivity, and horizontal dispersion coefficients are assumed to be constant in space and time in our model. Varying these coefficients with bathymetry would lead to a different response to changes in bathymetry.

We present here recommendations on how to improve these model aspects, to gain more insight into the salt dynamics in estuarine networks. To improve the description of tidal salt transport, additional mechanisms that generate a phase difference between tidal currents and salinity, for example, multiple tidal constituents (externally forced and internally generated), lateral effects (Scully and Geyer, 2012), or tidal trapping in side embayments (Okubo, 1973; Geyer and Signell, 1992; MacVean and Stacey, 2011), could be included. However, finding a suitable description of these processes in the simplified model may not be straightforward. Next, more realistic parametrisations of vertical eddy viscosity, vertical eddy diffusivity, and horizontal dispersion coefficients could be employed. Other studies argue that the vertical eddy viscosity and vertical eddy diffusivity coefficients increase with the strength of the tidal currents and with increasing depth of the channels and decrease with increasing stratification (Monismith et al., 2002; MacCready, 2007). These effects could be included to improve the description of the turbulence closure of the model. For the horizontal dispersion coefficient, different parametrisations are proposed (Banas et al., 2004; MacCready, 2007; Aristizábal and Chant, 2015). However, the use of these formulations in our model is hindered by the fact that we explicitly resolve part of the salt transport by the tidal current.

Another direction for future research is the inclusion of additional forcing conditions, for example, water level fluctuations at subtidal and intratidal timescales at the sea boundary (Kranenburg et al., 2022) and water extractions, which are on the order of $100\,\mathrm{m^3\,s^{-1}}$ (Huismans et al., 2024), about one-seventh of the total discharge in dry conditions.

5 Conclusions

The main findings, based on simulations with our idealised, partly analytical, 2DV model of an estuarine network, are the following:

1. The network model, when calibrated, has satisfactory agreement with observations, despite missing potentially important aspects of the salinity dynamics. The reason for this is that the salt transport associated with these aspects projects well onto the calibrated processes, especially onto the horizontal salt dispersion. A consequence is that local variations in the salt transport due to tidal currents are only crudely resolved.

2. Salt transport components related to different mechanisms vary in relative importance within a network due to differences in water depth, discharge, phases of the tidal currents, and characteristics of the salt field itself. In the deeper channels of the RMD, upstream salt transport by exchange flow is dominant, but in the shallower parts, tidal dispersion takes over. Salt transport by tidal currents can be directed seawards around a junction when the currents of the different channels are out of phase.

3. Channels closer to the estuary mouth respond faster to changes in discharge than those further upstream. The response to an increase in discharge is faster than the response to a decrease, in agreement with theory of single-channel estuaries. Channels that receive little discharge have large response times, especially when the net water transport is zero.

4. The impact of changes in the depth of an individual channel in a network on the extent of salt intrusion into the major branches depends on where the change takes place. The impact is determined by the direct, local effect on factors such as the strength of the exchange flow and the interaction with other channels, which is related to changes in the distribution of discharge and tidal currents. Scaling relationships developed for single-channel estuaries are found to be invalid for depth changes in an estuarine network. Salt intrusion into a channel with lower discharge is more sensitive to changes in depth than into a channel with higher discharge. The phase differences in tidal currents around a junction are sensitive to changes in the depth, and this sensitivity can be the cause of changes in salt intrusion when the depth of a channel in another part of the network is changed.

Appendix A: Geometry of the Rhine–Meuse Delta

Table A1. Geometry of the Rhine–Meuse Delta used in the model. The abbreviations correspond to Fig. 2. The widths at the boundaries of the channels are provided here; the widths in the interior are computed using Eq. 1.

Channel	Abbreviation	Depth [m]	Length [km]	Initial width [m]	Final width [m]
Beneden Merwede	BM	6	15.3	100	300
Breeddiep	BD	16	2.5	1200	1200
Dordtsche Kil	DK	10.7	9.4	300	300
Haringvliet	HV	8.7	11.7	2420	2420
Hartelkanaal	HK	7.6	25.8	310	1500
Hollands Diep 1	HD1	7.6	32.0	1630	2000
Hollands Diep 2	HD2	6.2	3.81	1600	1100
Hollandse IJssel	HY	4.0	19.7	45	150
Lek	LE	5.3	42.0	136	260
Maas	MA	5.3	62.3	97	416
Nieuwe Maas 1	NM1	11	18.75	400	500
Nieuwe Maas 2	NM2	8.1	4.9	250	400
Nieuwe Merwede	NM	5	19.6	400	730
Nieuwe Waterweg	RW	16	16.8	600	600
Noord	NO	7	8.6	250	220
Oude Maas 1	OM1	13	3.1	250	250
Oude Maas 2	OM2	14	8.25	317	317
Oude Maas 3	OM3	10.2	15	240	350
Oude Maas 4	OM4	7	4.26	250	250
Spui	SP	6.4	17.4	250	250
Waal	WA	4	45.2	214	500

Appendix B: Conditions at internal boundaries

There are two types of internal boundaries in the model: connections between segments and junctions. The conditions below are given for junctions. For connections between segments, the same conditions apply, but only two channels are considered. The conditions for hydrodynamics at the internal boundaries read

$$\sum_{p=1}^{3} b_p H_p \overline{u}_{\text{st},p} = 0, \quad \eta_{\text{st},1} = \eta_{\text{st},2} = \eta_{\text{st},3},$$

$$\sum_{p=1}^{3} b_p H_p \overline{u}_{\text{ti},p} = 0, \quad \eta_{\text{ti},1} = \eta_{\text{ti},2} = \eta_{\text{ti},3}, \tag{B1}$$

where subscripts 1, 2, and 3 are indices of the channels that are connected to the junction. Regarding salinity, continuity of salt transport and salinity is used at every vertical level, which reads

$$\sum_{p=1}^{3} T_p = 0, \quad \overline{s}_{\text{st},1} = \overline{s}_{\text{st},2} = \overline{s}_{\text{st},3}, \tag{B2a}$$

$$\sum_{p=1}^{3} b_p H_p \left(u'_{\text{st},p} s'_{\text{st},p} - \overline{u'_{\text{st},p} s'_{\text{st},p}} \right.$$

$$\left. + \left(u'_{\text{ti},p} s'_{\text{ti},p} - \overline{u'_{\text{ti},p} s'_{\text{ti},p}} \right)_{\text{st}} - K_{\text{h,st}} \frac{\partial s'_{\text{st},p}}{\partial x} \right) = 0,$$

$$s'_{\text{st},1} = s'_{\text{st},2} = s'_{\text{st},3}, \tag{B2b}$$

$$\sum_{p=1}^{3} b_p H_p \left(u_{\text{ti},p} s_{\text{ti},p} + u_{\text{ti},p} s_{\text{ti},p} - K_{\text{h,ti}} \frac{\partial s_{\text{ti},p}}{\partial x} \right) = 0,$$

$$s_{\text{ti},1} = s_{\text{ti},2} = s_{\text{ti},3}. \tag{B2c}$$

Note that the conditions for the vertically varying quantities are evaluated at sigma levels (i.e. at $\tilde{z} = \frac{z}{H} = $ constant) when the channels have non-equal depths.

Appendix C: Boundary layer correction for salinity at junctions

The first-order equation for tidally varying salinity s_{ti} reads (Biemond et al., 2024a)

$$\frac{\partial s_{\text{ti}}}{\partial t} + u_{\text{ti}} \frac{\partial \overline{s}_{\text{st}}}{\partial x} + w_{\text{ti}} \frac{\partial s'_{\text{st}}}{\partial z} = \frac{\partial}{\partial x} \left(K_{\text{h,ti}} \frac{\partial s_{\text{ti}}}{\partial x} \right) + \frac{\partial}{\partial z} \left(K_{\text{v,ti}} \frac{\partial s_{\text{ti}}}{\partial z} \right), \tag{C1}$$

in which t is time; u_{ti} and w_{ti} are the horizontal and vertical components of the tidal current, respectively; $\overline{s}_{\text{st}}$ is the depth and tidally averaged salinity; s'_{st} is the vertical distortion from the tidally averaged salinity; and $K_{\text{h,ti}}$ and $K_{\text{v,ti}}$ are the horizontal dispersion coefficient and vertical eddy diffusivity coefficient acting on the tidal salinity, respectively. The boundary conditions are no flux at the bottom and surface and Eq. (B2c) for the horizontal boundaries (junctions).

The horizontal dispersion term is included in Eq. (C1). In Wei et al. (2016) and Biemond et al. (2024a), it was argued that this term is small with respect to the other terms in this equation. We argue here that horizontal dispersion is important in the neighbourhood of junctions, as tidal currents are observed to be more turbulent close to junctions (Corlett and Geyer, 2020), which increases the magnitude of dispersion. Moreover, when horizontal dispersion is excluded, Eq. (C1) does not contain horizontal derivatives of s_{ti}, which implies that no horizontal boundary conditions can be applied, and therefore the continuity of salinity at the junctions cannot be imposed.

To develop a set of equations that takes horizontal dispersion into account around the junctions, we scale Eq. (C1) by defining

$$t = \omega^{-1} \tilde{t}, \ x = L\tilde{x}, \ z = H\tilde{z}, \ u_{\text{ti}} = U\tilde{u}_{\text{ti}},$$

$$w_{\text{ti}} = H\omega \, \tilde{w}_{\text{ti}}, \ s_{\text{st}} = S_{\text{st}}\tilde{s}_{\text{st}}, \ s_{\text{ti}} = \frac{U S_{\text{st}}}{\omega L} \tilde{s}_{\text{ti}}. \tag{C2}$$

In these expressions, ω is the frequency of the tide, L is the horizontal length scale on which s_{ti} varies (when not being affected by junctions), U is the magnitude of the tidal current, and S_{st} is a typical scale for the subtidal salinity. The last condition follows from $\frac{\partial s_{\text{ti}}}{\partial t} \approx u_{\text{ti}} \frac{\partial s_{\text{st}}}{\partial x}$ (Biemond et al., 2024a). This yields, after dropping the tildes,

$$\frac{\partial s_{\text{ti}}}{\partial t} + u_{\text{ti}} \frac{\partial \overline{s}_{\text{st}}}{\partial x} + \chi_1 w_{\text{ti}} \frac{\partial s'_{\text{st}}}{\partial z} = \varepsilon \frac{\partial^2 s_{\text{ti}}}{\partial x^2} + \chi_2 \frac{\partial^2 s_{\text{ti}}}{\partial z^2}, \tag{C3}$$

with $\chi_1 = \frac{L\omega}{U}$, $\chi_2 = \frac{K_{\text{v}}}{\omega H^2}$, and $\varepsilon = \frac{K_{\text{h}}}{\omega L^2}$. We write tidally varying salinity as $s_{\text{ti}} = \Re\left[\hat{s}_{\text{ti}} \exp(-i\omega t) + c.c.\right]$ (see Sect. 2.3) and find the equation

$$\chi_2 \frac{\partial^2 \hat{s}_{\text{ti}}}{\partial z^2} + i\hat{s}_{\text{ti}} + \varepsilon \frac{\partial^2 \hat{s}_{\text{ti}}}{\partial x^2} = \hat{u}_{\text{ti}} \frac{\partial \overline{s}_{\text{st}}}{\partial x} + \chi_1 \hat{w}_{\text{ti}} \frac{\partial s'_{\text{st}}}{\partial z}. \tag{C4}$$

When choosing typical scales for an estuary ($H = 10\,\text{m}$, $L = 10\,\text{km}$, $U = 1\,\text{m s}^{-1}$, $K_{\text{h,ti}} = 25\,\text{m s}^{-2}$, $K_{\text{v,ti}} = 0.01\,\text{m s}^{-2}$, and $\omega = 1.4 \times 10^{-4}\,\text{s}^{-1}$), it is found that χ_1 and χ_2 are on the same order (1), and ε is a factor of 10^3 smaller. This defines a singular perturbation problem, which is solved using standard techniques (see e.g. Eckhaus, 2011).

To construct the regular solution, we write

$$\hat{s}_{\text{ti,reg}} = \sum_{n=0}^{\infty} \varepsilon^n \phi_n. \tag{C5}$$

Inserting this into Eq. (C4) and collecting the first-order terms give Eq. (10), as is expected, which is valid outside the neighbourhood of the junctions. Close to the junctions, we look for a correction to this equation resulting from the horizontal dispersion. We write $\psi = \hat{s}_{\text{ti}} - \hat{s}_{\text{ti,reg}}$ and substitute this, which yields

$$\chi_2 \frac{\partial^2 \psi}{\partial z^2} + i\psi + \varepsilon \frac{\partial^2 \psi}{\partial x^2} = -\chi_2 \frac{\partial^2 \hat{s}_{\text{ti,reg}}}{\partial z^2} - i\hat{s}_{\text{ti,reg}}$$

$$- \varepsilon \frac{\partial^2 \hat{s}_{\text{ti,reg}}}{\partial x^2} + u_{\text{ti}} \frac{\partial \overline{s}_{\text{st}}}{\partial x} + \chi_1 w_{\text{ti}} \frac{\partial s'_{\text{st}}}{\partial z}. \tag{C6}$$
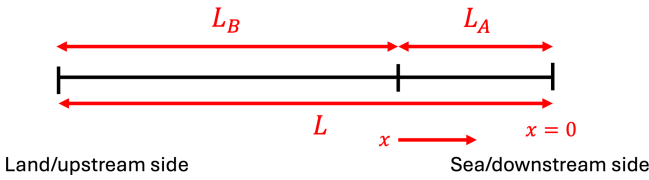
Figure D1. A sketch of the domain used in Appendix D.

We perform an expansion for the perturbation, i.e. $\psi = \sum_{n=0}^{\infty} \varepsilon^n \psi_n$. The first-order solution then reads

$$\chi_2 \frac{\partial^2 \psi_0}{\partial z^2} + i \psi_0 + \varepsilon \frac{\partial^2 \psi_0}{\partial x^2} = 0. \tag{C7}$$

Now a boundary layer coordinate ζ is introduced; i.e. we write $\psi_0 = B(z)e^\zeta$, with $\zeta = \pm \frac{x}{\varepsilon^\nu}$. It follows that $\nu = \frac{1}{2}$ when the horizontal dispersion term is of equal magnitude to the other terms in Eq. (C7). Substitution of this gives the following equation for $B(z)$:

$$\chi_2 \frac{d^2 B}{dz^2} + iB + B = 0. \tag{C8}$$

The no-flux boundary conditions at the bottom and surface apply to this equation. This is a homogenous problem, which has the solution

$$B(z) = \sum_{m=0}^{\infty} B_m \cos\left(m\pi \frac{z}{H}\right). \tag{C9}$$

The values of B_m follow from the horizontal boundary conditions associated with the junction (Eq. B2c). With this, we have a solution for tidally varying salinity in the neighbourhood of the junctions (the extent of this region is determined by $\varepsilon^{\frac{1}{2}}$), which accounts for increased dispersion around the junctions and obeys the horizontal boundary conditions. We set $K_{h,ti} = 25\,\mathrm{m^2\,s^{-1}}$; sensitivity tests indicate that the model skill is insensitive to this value.

Appendix D: Derivation of the dependence of salt intrusion on the sign of the change in depth

To explain why an increase in depth of the Rotterdam Waterway (RW) has a smaller effect on salt intrusion in the Nieuwe and Oude Maas than a decrease, we develop a set of equations to study the differences between changing the depth of the downstream part of a channel versus the depth of the entire channel.

Suppose that we have a single-channel estuary with constant width in equilibrium, where the salt import is governed by exchange flow, as in the RW. In that case, the terms T_Q and T_E in Eq. (11) balance each other. If we furthermore assume that stratification is the result of a balance between advection of $\bar{s}_{st}$ by the depth-dependent part of the subtidal current and

vertical eddy diffusion (Pritchard, 1954), the following equation for depth-averaged subtidal salinity $\bar{s}_{st}$ holds (Chatwin, 1976):

$$\frac{Q}{bH} \bar{s}_{st} = \frac{0.112}{48^2} \frac{g^2 \beta^2 H^8}{A_{v,st}^2 K_{v,st}} \left(\frac{\partial \bar{s}_{st}}{\partial x}\right)^3. \tag{D1}$$

The domain is shown in Fig. D1, and the associated boundary condition is $\bar{s}_{st} = s_{oc}$ at $x = 0$.

In a single-channel estuary with length L and constant width, this equation has an analytical solution for salinity, which reads

$$\bar{s}_{st} = s_{sc} \left(\left(\frac{s_{oc}}{s_{sc}}\right)^{\frac{2}{3}} + \frac{2}{3} \frac{x}{L_e}\right)^{\frac{3}{2}} \text{ with}$$

$$L_e = \left(\frac{0.112}{48^2} \frac{bH}{Q} \frac{g^2 \beta^2 s_{sc}^2 H^8}{A_{v,st}^2 K_{v,st}}\right)^{\frac{1}{3}}, \tag{D2}$$

where we have introduced the salinity scale s_{sc}. To be able to change the depth of the downstream part of the channel separately, the single-channel estuary is divided into two segments with lengths L_A and L_B (see Fig. D1). In these segments, Eq. (D2) with $L_e \to L_{e,A}$, the value of L_e in domain A, is valid for segment A, and for segment B we have

$$\bar{s}_{st} = s_{sc} \left(\left(\frac{s_{oc}}{s_{sc}}\right)^{\frac{2}{3}} - \frac{2}{3} \frac{L_A}{L_{e,A}} + \frac{2}{3} \frac{(x + L_A)}{L_{e,B}}\right)^{\frac{3}{2}}, \tag{D3}$$

where we have used the continuity of salinity at the segment boundary (see Eq. B2a). Note that the values for $L_{e,A}$ and $L_{e,B}$ are different when the depths of the segments differ. From these expressions, we can find the position of a certain isohaline X_2 where salinity equals $s_{tres} = 2\,\mathrm{g\,kg^{-1}}$. This yields, for a single-segment estuary,

$$X_2 = \frac{3}{2} L_e \left(\left(\frac{s_{oc}}{s_{sc}}\right)^{\frac{2}{3}} - \left(\frac{s_{tres}}{s_{sc}}\right)^{\frac{2}{3}}\right). \tag{D4}$$

For an estuary consisting of two segments, Eq. (D4) (with $L_e \to L_{e,A}$) is also valid if the salt intrusion is confined to the first segment. In the case that X_2 is located in segment B, it follows that

$$X_2 = L_A + \frac{3}{2} L_{e,B} \left(\left(\frac{s_{oc}}{s_{sc}}\right)^{\frac{2}{3}} - \left(\frac{s_{tres}}{s_{sc}}\right)^{\frac{2}{3}} - \frac{2}{3} \frac{L_A}{L_{e,A}}\right). \tag{D5}$$

These expressions allow us to study the effect of changes in the depth of the entire channel and changes in the depth of only the downstream segment.

Code and data availability. The software used in this study is made available online (Biemond, 2024). More recent versions of

the model, called IMSIDE (Idealised Model of Salt Intrusion in Deltas and Estuaries), are available at https://github.com/nietBouke/IMSIDE (Biemond, 2024). The observational data used can be downloaded from https://waterinfo.rws.nl (Rijkswaterstaat, 2024).

References

Aristizábal, M. F. and Chant, R. J.: An observational study of salt fluxes in Delaware Bay, J. Geophys. Res.-Ocean., 120, 2751–2768, https://doi.org/10.1002/2014JC010680, 2015.

Banas, N. S., Hickey, B. M., MacCready, P., and Newton, J. A.: Dynamics of Willapa Bay, Washington: A highly unsteady, partially mixed estuary, J. Phys. Oceanogr., 34, 2413–2427, https://doi.org/10.1175/JPO2637.1, 2004.

Bellafiore, D., Ferrarin, C., Maicu, F., Manfè, G., Lorenzetti, G., Umgiesser, G., Zaggia, L., and Levinson, A. V.: Saltwater intrusion in a Mediterranean delta under a chang-ing climate, J. Geophys. Res.-Ocean., 126, e2020JC016437, https://doi.org/10.1029/2020JC016437, 2021.

Biemond, B.: Software for "Dynamics of salt intrusion in complex estuarine networks; an idealised model applied to the Rhine-Meuse Delta" (Version 4.3.6), Zenodo [code], https://doi.org/10.5281/zenodo.12793378, 2024.

Biemond, B., de Swart, H. E., Dijkstra, H. A., and Díez-Minguito, M.: Estuarine salinity response to freshwater pulses, J. Geophys. Res.-Ocean., 127, e2022JC018669, https://doi.org/10.1029/2022JC018669, 2022.

Biemond, B., de Swart, H. E., and Dijkstra, H. A.: Mechanisms of salt overspill at estuarine network junctions explained with an idealized model, J. Geophys. Res.-Ocean., 128, e2023JC019630, https://doi.org/10.1029/2023JC019630, 2023.

Biemond, B., de Swart, H. E., and Dijkstra, H. A.: Quantification of salt transports due to exchange flow and tidal flow in estuaries, J. Geophys. Res.-Ocean., 129, e2024JC021294, https://doi.org/10.1029/2024JC021294, 2024a.

Biemond, B., Vuik, V., Lambregts, P., de Swart, H. E., and Dijkstra, H. A.: Salt intrusion and effective longitudinal dispersion in man-made canals, a simplified model approach, Estuar. Coast. Shelf Sci., 298, 108654, https://doi.org/10.1016/j.ecss.2024.108654, 2024b.

Bowen, M. M. and Geyer, W. R.: Salt transport and the time-dependent salt balance of a partially stratified estuary, J. Geophys. Res.-Ocean., 108, 3158, https://doi.org/10.1029/2001JC001231, 2003.

Bricheno, L. M., Wolf, J., and Sun, Y.: Saline intrusion in the Ganges-Brahmaputra-Meghna megadelta, Estuar. Coast. Shelf Sci., 252, 107246, https://doi.org/10.1016/j.ecss.2021.107246, 2021.

Buschman, F. A., Hoitink, A. J. F., van der Vegt, M., and Hoekstra, P.: Subtidal flow division at a shallow tidal junction, Water Resour. Res., 46, W12515, https://doi.org/10.1029/2010WR009266, 2010.

Chatwin, P.: Some remarks on the maintenance of the salinity distribution in estuaries, Estuar. Coast. Mar. Sci., 4, 555–566, https://doi.org/10.1016/0302-3524(76)90030-X, 1976.

Chen, S.-N.: Asymmetric estuarine responses to changes in river forcing: A consequence of nonlinear salt flux, J. Phys. Oceanogr., 45, 2836–2847, https://doi.org/10.1175/JPO-D-15-0085.1, 2015.

Corlett, W. B. and Geyer, W. R.: Frontogenesis at Estuarine Junctions, Estuar. Coast., 43, 722–738, https://doi.org/10.1007/s12237-020-00697-1, 2020.

Cox, J. R., Huismans, Y., Knaake, S. M., Leuven, J. R. F. W., Vellinga, N. E., van der Vegt, M., Hoitink, A. J. F., and Kleinhans, M. G.: Anthropogenic Effects on the Contemporary Sediment Budget of the Lower Rhine-Meuse Delta Channel Network, Earth's Future, 9, e2020EF001869, https://doi.org/10.1029/2020EF001869, 2021.

Davies, A. M. and Jones, J. E.: Sensitivity of Tidal Bed Stress Distributions, Near-Bed Currents, Overtides, and Tidal Residuals to Frictional Effects in the Eastern Irish Sea, J. Phys. Oceanogr., 26, 2553–2575, https://doi.org/10.1175/1520-0485(1996)026<2553:SOTBSD>2.0.CO;2, 1996.

de Nijs, M. A. and Pietrzak, J. D.: Saltwater intrusion and ETM dynamics in a tidally-energetic stratified estuary, Ocean Model., 49/50, 60–85, https://doi.org/10.1016/j.ocemod.2012.03.004, 2012.

Dijkstra, Y. M. and Schuttelaars, H. M.: A unifying approach to subtidal salt intrusion modeling in tidal estuaries, J. Phys. Oceanogr., 51, 147–167, https://doi.org/10.1175/JPO-D-20-0006.1, 2021.

Eckhaus, W.: Asymptotic analysis of singular perturbations, Elsevier, ISBN-10: 0444853065, ISBN-13: 978-0444853066, 2011.

Eslami, S., Hoekstra, P., Kernkamp, H. W. J., Nguyen Trung, N., Do Duc, D., Nguyen Nghia, H., Tran Quang, T., van Dam, A., Darby, S. E., Parsons, D. R., Vasilopoulos, G., Braat, L., and van der Vegt, M.: Dynamics of salt intrusion in the Mekong Delta: results of field observations and integrated coastal–inland modelling, Earth Surf. Dynam., 9, 953–976, https://doi.org/10.5194/esurf-9-953-2021, 2021.

Garcia, A. M. P., Geyer, W. R., and Randall, N.: Exchange Flows in Tributary Creeks Enhance Dispersion by Tidal Trapping, Estuar. Coast., 45, 363–381, https://doi.org/10.1007/s12237-021-00969-4, 2022.

Geyer, W. R. and MacCready, P.: The estuarine circulation, Annu. Rev. Fluid Mech., 46, 175–197, https://doi.org/10.1146/annurev-fluid-010313-141302, 2014.

Geyer, W. R. and Signell, R. P.: A reassessment of the role of tidal dispersion in estuaries and bays, Estuaries, 15, 97–108, https://doi.org/10.2307/1352684, 1992.

Godin, G.: Compact approximations to the bottom friction term, for the study of tides propagating in channels, Cont. Shelf Res., 11, 579–589, https://doi.org/10.1016/0278-4343(91)90013-V, 1991.

Godin, G.: The propagation of tides up rivers with special considerations on the upper Saint Lawrence River, Estuar. Coast. Shelf Sci., 48, 307–324, https://doi.org/10.1006/ecss.1998.0422, 1999.

Gong, W., Maa, J. P.-Y., Hong, B., and Shen, J.: Salt transport during a dry season in the Modaomen Estuary, Pearl River Delta, China, Ocean Coast. Manag., 100, 139–150, https://doi.org/10.1016/j.ocecoaman.2014.03.024, 2014.

Huismans, Y. and Plieger, R.: Verondieping Oude Maas als potentiele maatregel tegen verzilting: een verkenning, Tech. rep., Deltares, 11202241-003-ZWS-0003, 2019 (in Dutch).

Huismans, Y., Leummens, L., Rodrigo, S., Laan, S., Kranenburg, W., and van der WIjk, R.: Extra debiet over stuw Hagestein voor het tegengaan van verzilting van de Lek, Tech. rep., Deltares, 11210363-001-ZKS-0001, 2024 (in Dutch).

Kolb, P., Zorndt, A., Burchard, H., Gräwe, U., and Kösters, F.: Modelling the impact of anthropogenic measures on saltwater intrusion in the Weser estuary, Ocean Sci., 18, 1725–1739, https://doi.org/10.5194/os-18-1725-2022, 2022.

Kranenburg, W., Van der Kaaij, T., Tiessen, M., Friocourt, Y., and Blaas, M.: Salt intrusion in the Rhine Meuse Delta: Estuarine circulation, tidal dispersion or surge effect, in: Proceedings of the 39th IAHR World Congress, 19–24 June 2022, Granada, Spain, International Association for Hydro-Environment Engineering and Research (IAHR), 5601–5608, https://doi.org/10.3850/IAHR-39WC2521711920221058, 2022.

Laan, S., Chavarrias, V., Huismans, Y., and van der Wijk, R.: Verzilting Hollandsche IJssel en Lek, Tech. rep., Deltares, 11206830-017-ZWS-0001, 2021 (in Dutch).

Laan, S., Huismans, Y., Rodrigo, S., Leummens, L., and Kranenburg, W.: Effect bodemligging op verzilting Nieuwe Waterweg, Nieuwe Maas en Lek, Tech. rep., Deltares, 11208075-010-ZWS-0001, 2023 (in Dutch).

Liu, C., Yu, M., Jia, L., Cai, H., and Chen, X.: Impacts of physical alterations on salt transport during the dry season in the Modaomen Estuary, Pearl River Delta, China, Estuar. Coast. Shelf Sci., 227, 106345, https://doi.org/10.1016/j.ecss.2019.106345, 2019.

Liu, J., Hetland, R., Yang, Z., Wang, T., and Sun, N.: Response of salt intrusion in a tidal estuary to regional climatic forcing, Environ. Res. Lett., 19, 074019, https://doi.org/10.1088/1748-9326/ad4fa1, 2024.

MacCready, P.: Toward a unified theory of tidally-averaged estuarine salinity structure, Estuaries, 27, 561–570, https://doi.org/10.1007/BF02907644, 2004.

MacCready, P.: Estuarine adjustment, J. Phys. Oceanogr., 37, 2133–2145, https://doi.org/10.1175/JPO3082.1, 2007.

MacVean, L. J. and Stacey, M. T.: Estuarine Dispersion from Tidal Trapping: A New Analytical Framework, Estuar. Coast., 34, 45–59, https://doi.org/10.1007/s12237-010-9298-x, 2011.

Maicu, F., De Pascalis, F., Ferrarin, C., and Umgiesser, G.: Hydrodynamics of the Po River-Delta-Sea System, J. Geophys. Res.-Ocean., 123, 6349–6372, https://doi.org/10.1029/2017JC013601, 2018.

Martyr-Koller, R., Kernkamp, H., van Dam, A., van der Wegen, M., Lucas, L., Knowles, N., Jaffe, B., and Fregoso, T.: Application of an unstructured 3D finite volume numerical model to flows and salinity dynamics in the San Francisco Bay-Delta, Estuar. Coast. Shelf Sci., 192, 86–107, https://doi.org/10.1016/j.ecss.2017.04.024, 2017.

Monismith, S.: An integral model of unsteady salinity intrusion in estuaries, J. Hydraul. Res., 55, 392–408, https://doi.org/10.1080/00221686.2016.1274682, 2017.

Monismith, S., Kimmerer, W., Burau, J., and Stacey, M.: Structure and flow-induced variability of the subtidal salinity field in northern San Francisco Bay, J. Phys. Oceanogr., 32, 3003–3019, https://doi.org/10.1175/1520-0485(2002)032<3003:SAFIVO>2.0.CO;2, 2002.

Moriasi, D. N., Gitau, M. W., Pai, N., and Daggupati, P.: Hydrologic and water quality models: Performance measures and evaluation criteria, T. ASABE, 58, 1763–1785, https://doi.org/10.13031/trans.58.10715, 2015.

Murray, A. B.: Contrasting the goals, strategies, and predictions associated with simplified numerical models and detailed simulations, Geophys. Monogr.-Am. Geophys. Union, 135, 151–168, https://doi.org/10.1029/135GM11, 2003.

Nash, J. and Sutcliffe, J.: River flow forecasting through conceptual models part I – A discussion of principles, J. Hydrol., 10, 282–290, https://doi.org/10.1016/0022-1694(70)90255-6, 1970.

Nguyen, A. D. and Savenije, H. H.: Salt intrusion in multi-channel estuaries: a case study in the Mekong Delta, Vietnam, Hydrol. Earth Syst. Sci., 10, 743–754, https://doi.org/10.5194/hess-10-743-2006, 2006.

Okubo, A.: Effect of shoreline irregularities on streamwise dispersion in estuaries and other embayments, Neth. J. Sea Res., 6, 213–224, https://doi.org/10.1016/0077-7579(73)90014-8, 1973.

Pritchard, D. W.: A study of the salt balance in a coastal plain estuary, J. Mar. Res., 13, 133–144, 1954.

Qiu, C. and Zhu, J.: Assessing the Influence of Sea Level Rise on Salt Transport Processes and Estuarine Circulation in the Changjiang River Estuary, J. Coast. Res., 31, 661–670, https://doi.org/10.2112/JCOASTRES-D-13-00138.1, 2015.

Qiu, C. and Zhu, J.-R.: Influence of seasonal runoff regulation by the Three Gorges Reservoir on saltwater intrusion in

the Changjiang River Estuary, Cont. Shelf Res., 71, 16–26, https://doi.org/10.1016/j.csr.2013.09.024, 2013.

Ralston, D. K. and Geyer, W. R.: Response to Channel Deepening of the Salinity Intrusion, Estuarine Circulation, and Stratification in an Urbanized Estuary, J. Geophys. Res.-Ocean., 124, 4784–4802, https://doi.org/10.1029/2019JC015006, 2019.

Ralston, D. K., Geyer, W. R., and Lerczak, J. A.: Structure, variability, and salt flux in a strongly forced salt wedge estuary, J. Geophys. Res.-Ocean., 115, C06005, https://doi.org/10.1029/2009JC005806, 2010.

Rijkswaterstaat: Waterinfo, Rijkswaterstaat [data set], https://waterinfo.rws.nl/, last access: 31 January 2024.

Savenije, H. H.: Predictive model for salt intrusion in estuaries, J. Hydrol., 148, 203–218, https://doi.org/10.1016/0022-1694(93)90260-G, 1993.

Scully, M. E. and Geyer, W. R.: The Role of Advection, Straining, and Mixing on the Tidal Variability of Estuarine Stratification, J. Phys. Oceanogr., 42, 855–868, https://doi.org/10.1175/JPO-D-10-05010.1, 2012.

Siles-Ajamil, R., Díez-Minguito, M., and Losada, M.: Tide propagation and salinity distribution response to changes in water depth and channel network in the Guadalquivir River Estuary: An exploratory model approach, Ocean Coast. Manag., 174, 92–107, https://doi.org/10.1016/j.ocecoaman.2019.03.015, 2019.

Walters, R.: A model for tides and currents in the English Channel and southern North Sea, Adv. Water Resour., 10, 138–148, https://doi.org/10.1016/0309-1708(87)90020-0, 1987.

Wang, J., de Swart, H. E., and Dijkstra, Y. M.: Dependence of tides and river water transport in an estuarine network on river discharge, tidal forcing, geometry and sea level rise, Cont. Shelf Res., 225, 104476, https://doi.org/10.1016/j.csr.2021.104476, 2021.

Warner, J., Schoellhamer, D., Burau, J., and Schladow, G.: Effects of tidal current phase at the junction of two straits, Cont. Shelf Res., 22, 1629–1642, https://doi.org/10.1016/S0278-4343(02)00026-2, 2002.

Wei, X., Schramkowski, G. P., and Schuttelaars, H. M.: Salt dynamics in well-mixed estuaries: Importance of advection by tides, J. Phys. Oceanogr., 46, 1457–1475, https://doi.org/10.1175/JPO-D-15-0045.1, 2016.

Wei, X., Williams, M. E., Brown, J. M., Thorne, P. D., and Amoudry, L. O.: Salt Intrusion as a Function of Estuary Length in Periodically Weakly Stratified Estuaries, Geophys. Res. Lett., 49, e2022GL099082, https://doi.org/10.1029/2022GL099082, 2022.

Winterwerp, J. C.: Decomposition of the mass transport in narrow estuaries, Estuar. Coast. Shelf Sci., 16, 627–638, https://doi.org/10.1016/0272-7714(83)90075-6, 1983.

Wu, S., Cheng, H., Xu, Y., Li, J., and Zheng, S.: Decadal changes in bathymetry of the Yangtze River Estuary: Human impacts and potential saltwater intrusion, Estuar. Coast. Shelf Sci., 182, 158–169, https://doi.org/10.1016/j.ecss.2016.10.002, 2016.

Wullems, B. J. M., Brauer, C. C., Baart, F., and Weerts, A. H.: Forecasting estuarine salt intrusion in the Rhine–Meuse delta using an LSTM model, Hydrol. Earth Syst. Sci., 27, 3823–3850, https://doi.org/10.5194/hess-27-3823-2023, 2023.

Xue, P., Chen, C., Ding, P., Beardsley, R. C., Lin, H., Ge, J., and Kong, Y.: Saltwater intrusion into the Changjiang River: A model-guided mechanism study, J. Geophys. Res.-Ocean., 114, C02006, https://doi.org/10.1029/2008JC004831, 2009.

Zhang, E., Savenije, H. H., Wu, H., Kong, Y., and Zhu, J.: Analytical solution for salt intrusion in the Yangtze Estuary, China, Estuar. Coast. Shelf Sci., 91, 492–501, https://doi.org/10.1016/j.ecss.2010.11.008, 2011.

Zhu, J., Ding, P., Zhang, L., Wu, H., and Cao, H.: Influence of the deep waterway project on the Changjiang Estuary, in: The environment in Asia Pacific harbours, Springer, 79–92, https://doi.org/10.1007/1-4020-3655-8_6, 2006.